Climate Dynamics (2026) 64:235
https://doi.org/10.1007/s00382-026-08171-7

ORIGINAL ARTICLE

Drivers of summer extreme temperature trends in Europe: insight from three major heat waves using flow analogues

Luca Famooss Paolini[1,2] · **Salvatore Pascale**[1] · **Paolo Ruggieri**[1] · **Erika Brattich**[1] · **Silvana Di Sabatino**[1]

Received: 6 April 2025 / Accepted: 8 April 2026

Abstract

The increasing frequency of summer extreme temperatures in Europe has been attributed to atmospheric and thermodynamic changes, alongside their interaction. However, the role of dynamic changes remains uncertain, and the mechanisms driving future extreme temperature trends are not fully understood. This study investigates historical and future trends in atmospheric analogues associated with three major European heat waves: the 2010 Russian, 1972 Scandinavian, and 2003 French events. Then, using a multi-model large ensemble of climate projections, we decompose trends in extreme temperature occurrences into thermodynamic, dynamic and interaction components and assess the effects of global warming, internal climate variability, and inter-model differences. Results show that extreme temperature occurrences linked to the 2003 French heat wave analogues increased during the historical period, primarily due to the thermodynamic component and increasing analogue frequency. Models only partially reproduce these trends due to the underestimation of dynamic contribution. In the future, all models project a further increase of extreme temperature occurrences, primarily driven by the interaction term, which mainly reflects the combined effect of the strong co-evolving long-term trends in thermodynamic and dynamic conditions. For the 2010 Russian and 1972 Scandinavian heat waves, no definitive conclusions can be drawn due to large uncertainties from internal climate variability and inter-model differences. These findings provide further insight into the mechanisms driving extreme temperature trends in western Europe and emphasize the importance of considering all sources of uncertainty for a robust evaluation of climate model projections.

1 Introduction

Summer extreme temperatures are among the most impactful meteoclimatic events, with the potential to cause significant damages to human health, the environment and socio-economic and biological systems (e.g., García-Herrera et al. 2010; Ebi et al. 2021). This aspect is particularly relevant in the context of climate change, as numerous studies have shown that the intensity, frequency, and duration of extreme temperatures have been increasing since the mid-20th century, and are expected to continue rising in the future (Lee et al. 2023). For example, Masselot et al. (2025) have recently shown that most European cities could experience up to a 50% increase in heat-related mortality in the future unless strong mitigation and adaptation measures are implemented.

The increasing trends in summer extreme temperatures in Europe have been attributed to both atmospheric dynamic changes and thermodynamic factors, as well as their mutual interaction through land–atmosphere feedbacks (Domeisen et al. 2023). Specifically, these trends have been partly explained by increased frequency and persistence of double jet stream configuration or anticyclonic atmospheric circulation over the continent (Horton et al. 2015; Rousi et al. 2022), which can induce heat extremes through the advection of warm air, adiabatic heating and increased solar radiation (Horton et al. 2016; Röthlisberger and Papritz 2023). The extreme temperature trends have been also linked to soil moisture drying and stronger land–atmosphere coupling across Europe (Seneviratne et al. 2010; Vogel et al. 2017). In particular, central and eastern Europe are transitioning towards a soil moisture-limited climate zone, in which surface temperatures are largely controlled by soil moisture variability

---

✉ Luca Famooss Paolini
luca.famoosspaolini@unibo.it

[1] Department of Physics and Astronomy "Augusto Righi", University of Bologna, Bologna, Italy

[2] Now at CMCC Foundation - Euro-Mediterranean Center on Climate Change, Bologna, Italy

and related feedback mechanisms (Seneviratne et al. 2006; Fischer et al. 2007). Moreover, changes in cloud cover and aerosol emissions have been shown to play a role, affecting the surface solar radiation (Ruckstuhl et al. 2008) and, thus, influencing heat extremes through radiative fluxes and soil moisture–radiation feedback (Vogel et al. 2017). As an example, the reduction of sulfate aerosol emissions since 1980 has been found to account for up to 25% of the historical surface warming trend (Nabat et al. 2014). Additionally, changes in thermal advection due to changes in temperature gradient have been shown to further enhance the surface temperature variability in some European regions (Holmes et al. 2016). All these factors must be considered alongside the rise in global mean temperature due to global warming, which further increases the likelihood of extreme temperature events by shifting the probability distribution of surface temperatures towards higher extreme values (Suarez-Gutierrez et al. 2020).

Despite these advancements, the relative contribution of the dynamic and thermodynamic factors and their interaction to future trends in European summer extreme temperatures is still debated. Indeed, previous studies have mostly focused on the historical period, without investigating how the partition of the extreme temperature trends will evolve under the influence of global warming (Horton et al. 2015; Rogers et al. 2022). In this context, the studies that have explored future trends have mostly focused on individual drivers (Donat et al. 2017; Vogel et al. 2017; Jézéquel et al. 2018a), lacking a comprehensive analysis of the mechanisms underlying these trends. On the other hand, the few studies that have considered multiple contributing factors have typically relied on single model frameworks or models with a limited number of ensemble members, which limits the ability to assess uncertainties associated with inter-model differences and internal climate variability (Suarez-Gutierrez et al. 2020). Furthermore, while there is large consensus on the changes of thermodynamic drivers and their influence on temperature extremes, the same cannot be said for dynamic changes (Shepherd 2014). Although several studies have reported increasing trends in the persistence and frequency of summer blocking events and anticyclonic circulation over Euro-Russian region (Francis and Vavrus 2012; Ruti et al. 2014; Jézéquel et al. 2018a; Vautard et al. 2023), other studies have not confirmed these trends, finding either opposite or not statistically significant trends (Barnes et al. 2014; Peings et al. 2017; Woollings et al. 2018). Similarly, previous studies have shown inconsistent results on potential changes in Rossby wave propagation, which has been proposed as another mechanism to explain trends in heat extremes. Indeed, the anticyclonic circulation that characterizes summer extreme temperatures across Europe may be associated with longitudinally confined as well as circumglobal wave-like structures that propagate along the extratropical and subtropical jet stream waveguides (e.g., Wolf et al. 2018; Kornhuber et al. 2019). In this context, some studies have suggested that the increased occurrence of extreme temperature events in Europe may be linked to a reduction in the eastward phase speed of Rossby waves, leading to more persistent anticyclonic circulation over the continent (Francis and Vavrus 2012; Kornhuber et al. 2019). However, other studies have found no systematic trends in the Rossby wave phase speed (Barnes 2013; Riboldi et al. 2020). Although these results are sensitive to the diagnostic adopted, nonetheless they highlight the low confidence in both past and future predicted changes in atmospheric dynamic.

Based on this evidence, we first assess the historical and future trends in the occurrence of atmospheric circulation patterns similar to those that triggered some of the most intense European heat waves in past decades. In order to do that, we adopt the atmospheric flow analogue technique, largely used in the literature to analyse the dynamic component of extreme events (e.g., Jézéquel et al. 2018b). Next, we decompose the historical and projected trends of European summer extreme temperatures associated with these patterns into thermodynamic, dynamic and interaction components, with the latter capturing the interplay between the first two. These analyses are conducted using a multi-model large ensemble (MMLE) dataset (Deser et al. 2020; Maher et al. 2021), under the "business-as-usual" emission scenario for future projections. This allows us to examine the role of the global warming, internal climate variability and model uncertainties on trends of European extreme temperature occurrences. Furthermore, this approach enables us to evaluate trends in events that share characteristics with the most significant heat waves of past decades.

The manuscript is structured as follows. In Sect. 2 we describe the data, the atmospheric analogue approach, the trend partition technique, and the methodology adopted to investigate the physical meaning of the partition term capturing the thermodynamic–dynamic interaction. In Sect. 3, we present the dynamic trends of the three major heat waves from 1940 to 2022, that is the 2010 Russian, 1972 Scandinavian and 2003 French heat waves, followed by the partition of trends in summer extreme temperature occurrences associated with their atmospheric analogues. Then, we present a more detailed assessment of the interaction term for the 2003 French heat wave. Finally, in Sect. 4 we address some open issues arising from the findings of present work, and in Sect. 5 we summarize its most relevant results.

2 Data and methodological approach

2.1 Data

Previous studies analyzing extreme temperature trends have not accounted for result uncertainties arising from both inter-model differences and internal climate variability (e.g., Suarez-Gutierrez et al. 2020). In order to evaluate these two important sources of uncertainty, we analyse a MMLE dataset consisting of three single-model initial-condition large ensembles (SMILEs), part of the MMLE Archive at the National Center for Atmospheric Research (Deser et al. 2020), and three models from Coupled Model Intercomparison Project phase 6 (CMIP6) (Table 1). We specify that the SMILEs were run using CMIP5-class models, and therefore we will refer to as CMIP5 models throughout the text. We select only models available on public servers with more than 20 ensemble members, to assess the influence of internal climate variability (Deser et al. 2020). The model selection results in the subset of six climate models listed in Table 1, which we consider adequate to capture the uncertainty linked to inter-model differences. Furthermore, we select those simulations that provide all the variables of interest for both the historical and projection time periods. The variables of interest for the analyses described in the following sections are daily geopotential height at 500 hPa (Z500), daily maximum temperature at 2 m height (T2m_max), and monthly sensible latent heat fluxes (SHF). As a result, ensemble members with data available for only one time period, with incomplete coverage, or missing key variables are excluded from the analysis. In this context, it is specified that the daily temperature at 2 m height is used for the CMIP5 model from the Geophysical Fluid Dynamics Laboratory (second row in Table 1), as the T2m_max is not available on the server utilized to download its data. Finally, we use ERA5 atmospheric reanalysis as surrogate of observations (Hersbach et al. 2020).

2.2 Heat wave detection

In this study, we focus our analyses on summer extreme temperature events across Europe characterized by atmospheric circulation similar to those of the most significant heat waves in past decades. Specifically, we concentrate on those events detected from 1940 to 2022 in the ERA5 dataset. These heat waves are identified using the Heat Wave Magnitude Index daily (HWMId) as defined by Russo et al. (2015), a dimensionless number representing the highest heat wave magnitude recorded within a year at each grid point. This index is preferred over other indices commonly used for detecting heat wave events because it combines both duration and amplitude of extreme temperature anomalies into a single value, capturing the key characteristics needed to select the most impactful heat waves of past decades. The heat waves are ranked based on the maximum HWMId values over land across Europe (11° W–57°E; 36°N–71°N). The maximum HWMId values are obtained using HWMId values previously smoothed with a 2D spatial Gaussian–Kernel filter applied to a 7×7 grid point box and with standard deviation equal to 2. Following the methodological approach of previous studies (e.g., Famooss Paolini et al. 2022), this smoothing is applied in order to remove isolated grid points of intense HWMId not representative of large-scale heat wave events. In this context, it is important to specify that, because HWMId returns the annual peak at each grid point, neighboring cells can, in principle, reflect events occurring at different times of the year. This may raise concerns that spatial filtering could mix temporally incoherent signals and introduce artifacts in the heat wave ranking. However, heat waves are generally associated with synoptic-scale circulation patterns, exhibiting a certain degree of spatial coherence. Thus, nearby grid points are expected to experience their annual most extreme temperatures within a similar time window. Within this framework, the spatial smoothing applied here removes isolated

Table 1 MMLE dataset

CMIP phase	Institution	Model	Resolution (atmosphere/ocean)	Ensemble size	Members	References
CMIP5	CCCma	CanESM2	$\sim 2.8^\circ \times 2.8^\circ$ / $\sim 1.4^\circ \times 0.9^\circ$	48	r1i1p1f1–r50i1p1f1 (r4i1p1f1 and r7i1p1f1 excluded)	Kirchmeier-Young et al. (2017)
	GFDL	GFDL-CM3	$\sim 2.0^\circ \times 2.5^\circ$ / $\sim 1.0^\circ \times 0.9^\circ$	20	r1i1p1–r20i1p1	Sun et al. (2018)
	NCAR	CESM1-CAM5	$\sim 0.9^\circ \times 1.3^\circ$ / nominal 1.0°	35	r1i1p1–r35i1p1	Kay et al. (2015)
CMIP6	CCCma	CanESM5	$\sim 2.8^\circ \times 2.8^\circ$ / nominal 1.0°	20	r1i1p1f1–r10i1p1f1; r1i1p2f1–r10i1p2f1	Swart et al. (2019)
	EC-Earth	EC-Earth3	$\sim 0.7^\circ \times 0.7^\circ$ / nominal 1.0°	50	r101i1p1f1–r150i1p1f1	Wyser et al. (2021)
	MPI	MPI-ESM1-2-LR	$\sim 1.9^\circ \times 1.9^\circ$ / nominal 1.5°	49	r1i1p1f1–r50i1p1f1 (r33i1p1f1 excluded)	Olonscheck et al. (2023)

Columns detail the CMIP phase, institution name, model name, atmospheric and oceanic resolution, ensemble size, model members and model reference. The following acronyms are used for institution names: CCCma: Canadian centre for climate modelling and analysis; EC-Earth: EC-Earth-consortium; GFDL: Geophysical fluid dynamics laboratory; MPI: Max planck institute; NCAR: National centre for atmospheric research. Members not listed or excluded from the table are omitted from the analysis due to incomplete data or unavailability on public servers grid points of intense HWMId, while relying on data that are temporally coherent. This assumption has been explicitly verified in the context of this study and found to be most appropriate where HWMId values are particularly large and geographically extensive, i.e. for intense, large-scale and long-lasting heat waves, which are the focus of our analysis (not shown). Differently, the smoothing may be less suitable for detecting weaker or highly localized heat waves, since the spatial filtering may rely on neighboring HWMId values reflecting heat wave events occurring at different times of the year.

Table 2 lists the 10 most significant heat waves occurred during 1940–2022 in ERA5. Among them, we focus on the 2010 Russian, 1972 Scandinavian and 2003 French heat waves, which represent the three strongest heat waves of past decades. The 2010 and 2003 heat waves are included due to their exceptional climatic conditions, which set new European records in terms of spatial extent, duration, and temperature anomalies, and caused severe impacts such as widespread deaths, wildfires, crop failures, and economic losses (e.g., Barriopedro et al. 2011). For these reasons, the 2010 Russian and 2003 French heat waves are often referred to as “mega-heat waves”. The 1972 Scandinavian event, while also intense and impactful, is included because it has received comparatively less attention from the scientific community. Furthermore, its analysis could give important hints on the trends of extreme temperature occurrences at higher latitudes. Finally, we note that the analysis of these events offers hints about heat waves occurring in different European geographical regions, which may be characterized by distinct dynamic and thermodynamic properties.

Table 2 The 10 most significant heat waves in the ERA5 dataset during 1940–2022, ranked using the HWMId as defined by Russo et al. (2015)

Rank	Country	Year	Start date	Duration	Maximum HWMId
1	Russia	2010	July 10	41 days	54.15
2	Scandinavia	1972	June 26	21 days	41.78
3	France	2003	August 3	13 days	29.74
4	Balkans	1946	August 10	15 days	27.33
5	Turkey	2017	July 28	18 days	23.99
6	UK	1976	June 25	16 days	20.71
7	Spain	2022	July 10	10 days	20.70
8	Kazakhstan	1940	August 2	8 days	20.43
9	Scandinavia	2018	July 18	10 days	19.49
10	Turkey	2007	July 21	13 days	19.32

For each heat wave, columns detail the rank, the most affected country, the year of occurrence, the start date, the duration (days), and the local maximum HWMId over European land (11°W–57°E; 36°N–71°N). The maximum is extracted from HWMId values previously smoothed with a 2D spatial Gaussian–kernel filter. Refer to Sect. 2.2 for more detail

2.3 Atmospheric flow analogues

One objective of this work is to evaluate the trends in the occurrence of atmospheric circulation patterns that triggered the most intense heat waves in past decades. To do that, our analysis relies on atmospheric flow analogues, selecting days during the summer season (JJA) that exhibit atmospheric circulation patterns similar to those observed during the heat waves of interest. The latter are here defined by averaging the daily Z500 throughout the entire duration of each heat wave. The Z500 anomalies are calculated with respect to the daily Z500 climatology during the reference period 1981–2010. The similarity between Z500 maps is assessed through the Euclidean distance between the daily atmospheric circulation patterns and the reference patterns. This distance is computed as the square root of the sum of squared differences across all grid points within the region of interest (black boxes in Figs. 1b–3b). Finally, we identify the days characterized by an atmospheric analogue as those days having the Euclidean distance smaller than the 5^{th} percentile of all calculated distances during the historical period (1950–2022).

The event-mean Z500 anomalies are used as reference patterns for analogue detection because the heat waves considered here were characterized by persistent, quasi-stationary blocking conditions (Kornhuber et al. 2017, 2019). In this setting, the event-mean field approximates the leading circulation mode sustaining the heat waves, whereas the day-to-day fluctuations primarily represent the noise around this mode. Thus, comparing daily circulation to multi-day composites allows to target the slowly varying atmospheric component characterizing these extremes. This strategy aligns with previous studies relating daily circulation to composite/regime patterns (e.g., Cassano et al. 2007; Horton et al. 2015), but differ from other approaches that compare day-to-day fields directly (e.g., Jézéquel et al. 2018a). We prefer the former, because it isolates the most distinctive and stable signal that maintain heat waves, avoiding influence from transient features.

In this context, it is specified that the regions for calculating Euclidean distances are selected to capture the most important features of atmospheric flows for the development of surface extreme temperatures, that is the region of maximum positive Z500 anomalies. The selection of tailored domain for flow analogue analysis has been shown to be optimal for studying specific heat events, as it excludes large-scale features that do not directly influence regional extreme temperatures (Jézéquel et al. 2018b). Nevertheless, to evaluate the sensitivity of the results to the spatial extent of the analogue region, we also perform the analysis adopting an enlarged region for the calculation of Euclidean distances, thereby better capturing large-scale atmospheric

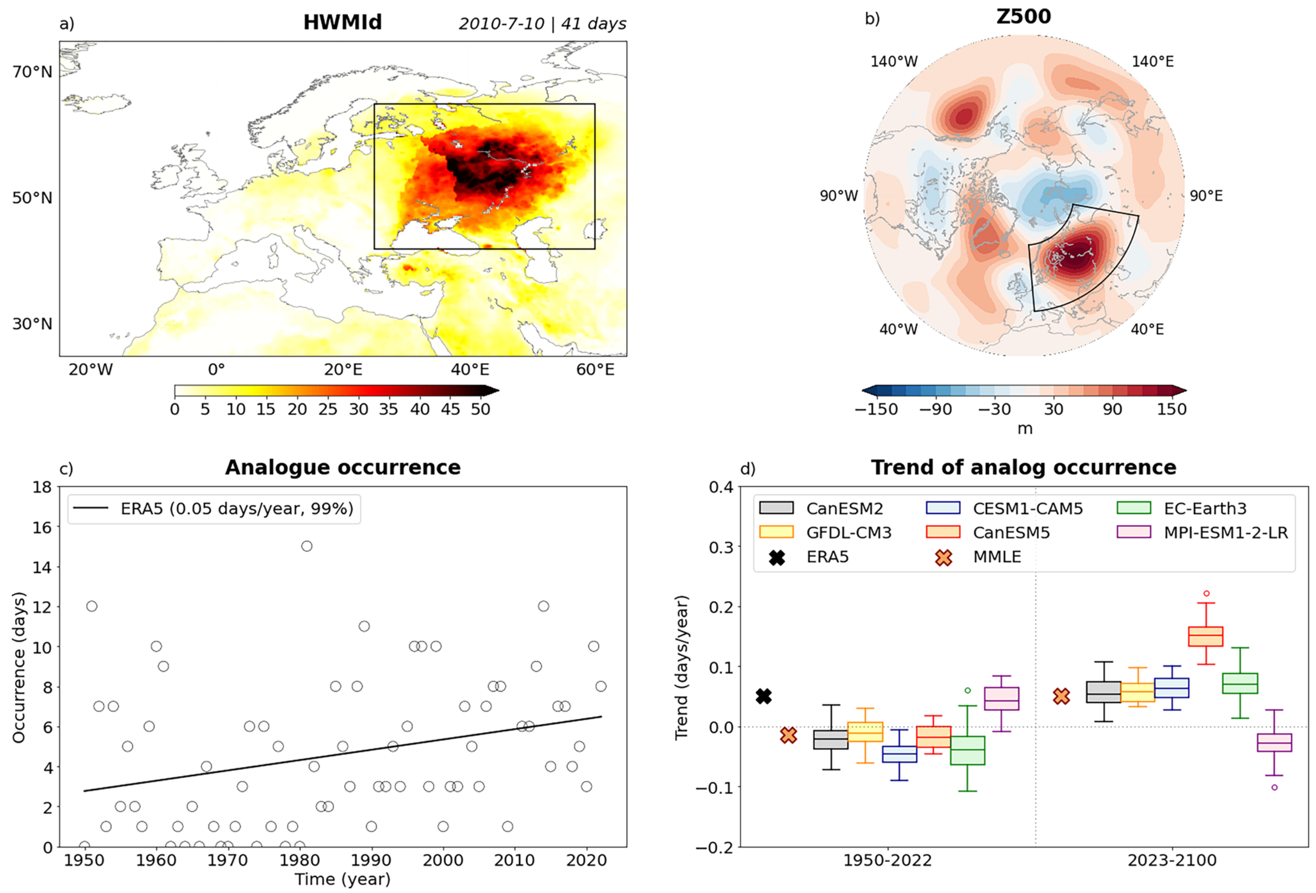

Fig. 1 **a** HWMId for the 2010 Russian heat wave in ERA5. The starting date and the duration of the heat wave are shown on the top right corner. The black box (25°E–60°E; 42°N–65°N) marks the region where the partition trend analysis is conducted for this heat wave. Refer to Sect. 2.4 for more detail about this analysis. **b** Z500 anomalies associated with the 2010 Russian heat wave, in the ERA5 dataset. These anomalies are calculated as daily Z500 departures from the 1981–2010 reference time period and averaged along the whole duration of the heat wave. The black box (5°W–80°W; 43°N–70°N) marks the region where the flow analogue technique is conducted for this heat wave. Refer to Sect. 2.3 for more detail about this analysis. **c** Occurrence of summer analogues (days; black circles) of the 2010 Russian heat wave atmospheric circulation, in the ERA5 dataset during the historical period (1950–2022). The black line represents the linear trend in analogue occurrence (days year^{-1}), with the trend value and its statistical significance provided in the upper left corner. **d** Trend of analogue occurrence (days year^{-1}) for ERA5 (black cross), MMLE mean (red cross) and single models (colored boxplots) during the historical (1950–2022) and projection (2023–2100) periods. The boxplots display the interquartile range, with the model mean indicated by the horizontal line inside each box. The whiskers extend to 1.5 times the interquartile range, and any outliers beyond this range are shown as individual circles

circulation features characterizing each heat wave analysed here. Finally, it is specified that, in order to calculate the Euclidean distances, the Z500 anomalies are linearly detrended to eliminate the effects of thermal expansion caused by global warming, which could potentially influence the search for analogues.

The trends in analogue occurrence are calculated via linear regression, using the analogue occurrence during each summer season (yearly data) as dependent variable and the years as independent variable. Analogues days from the same year as the event of interest are excluded from the estimation of analogue occurrence trend in the ERA5 dataset, to avoid the influence in the count of analogues caused by the atmospheric circulation persistence (Jézéquel et al. 2018a). The statistical significance of analogue trends is assessed using the non-parametric Mann-Kendall test, as modified by Hamed and Rao (1998) to consider potential autocorrelation of data. In this context, we take advantage of the pyMannKendall python package, created by Hussain and Mahmud (2019).

2.4 Partition of trends in the extreme temperature occurrences

Another key objective of this work is to evaluate the contribution of dynamic, thermodynamic and interaction components to trends in European extreme temperature occurrences, with a particular focus on events that share atmospheric circulation with the three most intense heat waves of past decades. To determine these contributions, we adopt a trend partition methodology similar to the one suggested by previous studies, such as Cassano et al. (2007) and Horton et al. (2015). Following the methodology, the timeseries of the number of summer extreme temperature days occurring during a specific analogue (*H*) can be written as follows:

$$H = h \cdot f = (\overline{h} + h') \cdot (\overline{f} + f') \quad (1)$$

where *h* is the number of extreme temperature days associated with a specific analogue divided by the number of days that the analogue occurs; *f* is the number of days that the analogue occurs; $\overline{h}$ is the climatological mean of *h*; h' is the timeseries of deviations from this climatology; $\overline{f}$ is the climatological mean of *f* and f' is the timeseries of deviations from it. The extreme temperature days are here defined as those when daily T2m_max exceeds the 90^{th} percentile of daily T2m_max during the summer season (JJA) computed over the 1981–2010 reference period.

Differentiating the equation above with respect to time and considering that the mean values are constant, we obtain:

$$\frac{dH}{dt} = \overline{f} \cdot \frac{dh'}{dt} + \overline{h} \cdot \frac{df'}{dt} + \frac{d(h' \cdot f')}{dt} \quad (2)$$

where the member on the left-hand side is the total trend in the number of extreme temperature days associated with a specific analogue, while the terms on the right-hand side represent the thermodynamic, dynamic and interaction contributions to the total trend, respectively. The thermodynamic term is calculated as the product of the mean frequency of a specific analogue and the trend in the frequency of extreme temperature days when the analogue occurs. This term represents the portion of the total trend due solely to changes in the fraction of analogue days characterized by extreme temperatures, independent of any changes in the frequency of the circulation pattern. The dynamic term is calculated as the product of the mean frequency of extreme temperature days when an analogue occurs and the trend in the analogue frequency. This term quantifies the portion of the total trend explained by changes in the frequency of the specific atmospheric circulation pattern, independent of any changes in the fraction of warm days associated with the analogue. Finally, the interaction term is defined as the trend of the product between the anomalies in both the fraction of analogue days characterized by extreme temperatures and the frequency of analogue occurrence. This term represents the portion of total trend explained by the interaction between the thermodynamic and dynamic components, and it has been suggested to capture the land–atmosphere coupling, primarily driven by feedback processes linked to soil moisture (Horton et al. 2015; Rogers et al. 2022). However, the studies that have used the partition analysis to assess extreme temperature trends have not performed any specific analysis to evaluate the connection between the interaction term and the land–atmosphere coupling. In this context, the physical interpretation of the interaction term has been questioned by Sui et al. (2020), which suggested that this term does not necessarily represent any particular physical process but may result or be randomly associated with various meteorological processes. To better understand the physical meaning of the interaction term, a more detailed analysis is conducted in this study. Refer to Sect. 2.5 for more detail.

The partition trend analysis described above is applied using number of summer extreme temperature days area-weighted averaged over those regions characterized by the greatest HWMId during the heat waves of interest (black box in Figs. 1a–3a). This approach allows us to better understand the role of the thermodynamic, dynamic and interaction components in explaining the trend of extreme temperature occurrences in the areas most affected by the strongest heat waves during 1940–2022. The anomalies of all the components in the two equations above are calculated respect the reference period 1981–2010, as for the Z500 data used for the flow analogue analysis. Finally, it is specified that all the trends in Eq. 2 are calculated via linear regression, using *H*, f', h' and $h' \cdot f'$ as dependent variables and the years as independent variable.

The contribution of the thermodynamic, dynamic and interaction terms is also expressed as percentage of the total trend for both ERA5 and the MMLE. In the case of the model datasets, the percentages are calculated for the model mean. This approach is used to prevent disproportionately high percentages for individual terms, which can occur not due to their actual intensity, but rather because many model members exhibit near-zero total trends, particularly during the historical period.

2.5 Decomposition of the interaction term and land–atmosphere coupling

As discussed in Sect. 2.4, the interaction term is defined as the trend of the product between h' and f', and it represents the interaction between the thermodynamic and dynamic components. Because it can be interpreted as a measure of their joint evolution, previous studies have suggested that it may capture nonlinear processes linking atmospheric circulation and temperature extremes, including land–atmosphere coupling (e.g., Horton et al. 2015). However, its physical interpretation has been questioned by other studies (e.g., Sui et al. 2020).

In order to better understand the physical meaning of the interaction term, we perform here an additional decomposition of the term. Since the anomalies in Eq. 2 are defined with respect to a fixed baseline climatology (1981–2010), any persistent change in the mean climate state may cause h' and f' to acquire non-zero means and long-term trends. In such cases, changes in the interaction term may arise not only from changes in the year-to-year covariance between h' and f', but also from (possibly uncorrelated) changes in their mean values induced by the evolving climate. This makes the interaction term sensitive to the methodology used to define the anomalies and, if not assessed in detail, may lead to misleading interpretations of its physical meaning. To disentangle this aspect, we decompose h' and f' into a linear trend component and a detrended component:

$$h' = h'_t + h'_d, \quad f' = f'_t + f'_d \tag{3}$$

where h'_t and f'_t denote the linear trends of these anomalies in time, and h'_d and f'_d are the corresponding detrended anomalies (i.e., fluctuations around the linear trend). As for Eq. 2, the linear trends are estimated via linear regression, using h' and f' as dependent variables and the years as independent variable. Then, the detrended anomalies are obtained as residuals from this fit.

Using this decomposition within $h' \cdot f'$ and differentiating with respect to time, we obtain:

$$\frac{d(h' \cdot f')}{dt} = \frac{d(h'_t \cdot f'_t)}{dt} + \frac{d(h'_d \cdot f'_d)}{dt} + \frac{d(h'_t \cdot f'_d)}{dt} + \frac{d(h'_d \cdot f'_t)}{dt} \tag{4}$$

In this framework, the first term on the right-hand side quantifies the portion of the interaction term that is explained by the co-evolving linear trends in h' and f'. The second term isolates the contribution from the covariance of the detrended anomalies, while the last two terms describe mixed contributions involving the trend of one variable and the detrended variability of the other. This decomposition allows us to assess how much of the interaction term is attributable to the changes in the mean of h' and f', which do not necessarily reflect any specific coupling process, and how much is instead associated with changes in their covariance, which can be more directly linked to physical processes such as the land–atmosphere coupling.

Building on this decomposition, we next investigate whether the interaction term is related to land–atmosphere coupling by comparing the $h'_d \cdot f'_d$ product with an independent land–atmosphere coupling diagnostic. Specifically, land–atmosphere coupling is assessed through the correlation between the summer SHF and the number of days an analogue occurs. As shown by Koster et al. (2016), diabatic heating anomalies associated with a dry land surface (i.e., enhanced SHF anomalies) can generate positive geopotential height anomalies above and near the heating source. These anomalies resemble atmospheric circulation patterns that drive surface extreme temperatures at extratropics. As a result, a positive feedback may develop between land conditions and atmospheric dynamics. Indeed, as negative soil moisture anomalies occur, the evapotranspiration decreases, resulting in enhanced SHF and a higher likelihood of extreme temperatures during an analogue (positive h'). In turn, the positive SHF anomalies increases the persistence of geopotential anomalies and the frequency of analogue occurrence (positive f'), further raising surface temperatures and intensifying soil moisture depletion. Consequently, a positive $h'_d \cdot f'_d$ product may emerge, associated with a positive correlation between the summer SHF and the number of days an analogue occurs. As such, stronger (weaker) land–atmosphere coupling is expected to result in a higher (lower) thermodynamic–dynamic product.

To explicitly connect the detrended covariance component of the interaction term with the land–atmosphere coupling, we compute the SHF–analogue correlation using a 30-year running window and compare it with the mean value of the $h'_d \cdot f'_d$ product over the same window. To ensure consistency with the detrending applied to h' and f', the SHF–analogue correlation is calculated from detrended SHF and analogue frequency data. The analysis is applied separately for the historical and projections periods. Definitions of the historical and projection periods are provided in Sect. 2.6. For each dataset (ERA5 and model ensembles), a least squares regression line is calculated by linearly regressing the land–atmosphere coupling diagnostic against the covariance component of the interaction term. The 95% confidence intervals of the linear regression are estimated using a bootstrap test performed 1000 times. The scatter plots enable us to evaluate potential changes in the strength of land–atmosphere coupling in the future, while the regression lines provide hints about its relationship with the interaction term (Figs. 8, S15, and S16).

2.6 Historical and projection periods

The atmospheric flow analogue analysis, trend partition, decomposition of the interaction term and land–atmosphere coupling assessment are conducted separately for the historical and projection periods. In this context, we define the historical period as 1950–2022 and the projection period as 2023–2100, focusing on the Representative Concentration Pathway 8.5 (RCP85) scenario for CMIP5 models and Shared Socioeconomic Pathways 5–8.5 (SSP585) scenario for CMIP6 models as the respective emission scenarios for the future. In the case of the EC-Earth3 model, members r101i1p1f1–r150i1p1f1 were only run from 1970 onward, so the historical period for this model is defined as 1970–2022.

The historical period as defined above allows for comparison of model results with ERA5 atmospheric reanalysis. It is specified that the historical runs for CMIP5 and CMIP6 models are run until 2005 and 2014 respectively, while the projection runs from 2006 and 2015 onwards. This means that the historical period is here built merging historical runs with the beginning of future projection runs. This aspect should not affect the results, because the effect of different emission scenarios starts to emerge after 20–30 years from the beginning of model simulations (Lee et al. 2021).

3 Results

3.1 Heat waves and atmospheric analogues

The most intense and long-lasting heat wave recorded in the European continent during 1940–2022 was the one that affected Russia in 2010 (Table 2). This heat wave began on July 10 and lasted approximately 41 days, with the HWMId reaching its maximum values in eastern Europe (Fig. 1a). The 2010 Russian heat wave was characterized by an "omega blocking" configuration, with intense positive Z500 anomalies extending from Scandinavian region to western Siberia and weak negative Z500 anomalies on the western and eastern flank of the Z500 height (Fig. 1b). Previous studies have linked this atmospheric configuration to recurrent (synoptic scale) wave packets repeatedly amplifying at the western flank of the block, which may have contributed to the onset of the heat wave (e.g., Fragkoulidis et al. 2018). Additionally, the Z500 anomalies have been associated to large-scale wave-like structures propagating along the summer upper-tropospheric polar and subtropical jet stream, such as the British–Baikal corridor and the circumglobal teleconnection patterns (Trenberth and Fasullo 2012; Xu et al. 2021). The local amplification of Z500 anomalies may have been driven by a double jet configuration that developed in the North Atlantic sector in early July, providing favorable conditions for quasi-resonant wave amplification and thereby intensifying the amplitude and intensity of wave ridge (Kornhuber et al. 2017).

Figure 1c shows that the occurrence of summer days with atmospheric circulation patterns similar to the 2010 Russian heat wave has increased over the historical period in ERA5, with a dynamic trend of 0.05 days year^{-1} (statistically significant at the 99% confidence level). In contrast, most of the models show a reduction in the occurrence of this analogue (Fig. S1), exhibiting a negative mean trend during the historical period (Fig. 1d). However, the individual model spread is particularly high, with trend values of single members fluctuating around zero and suggesting large internal climate variability. The inter-model spread is also large. Notably, MPI-ESM1-2-LR model mostly shows positive trend, consistent with observations but differing from the other models. Because of internal climate variability and inter-model spread, the MMLE mean trend exhibits a weak negative value. In contrast to the historical period, models exhibit more consistent results for future projections. Specifically, all CMIP5 models and two out of three CMIP6 models indicate an increase in analogue occurrence across all their ensemble members. This is not the case for MPI-ESM1-2-LR model, which shows a negative mean trend, with individual members displaying both positive and negative values. Despite that, the MMLE mean shows a positive mean trend, with value comparable to the ERA5 one during the historical period. In this context, it is worth noting that, because historical and projected trends oppose each other, the model ensemble mean of analogue days by 2100 is comparable to, or slightly higher than, its value at the start of the historical period (Fig. S1).

In agreement with previous studies (e.g., Jézéquel et al. 2018a), the results in Fig. 1d underscore a certain degree of uncertainty associated with the dynamic trend of the 2010 Russian heat wave, due to large inter-model spread and internal climate variability. Indeed, even if most models show a future positive trend in the occurrence of this atmospheric analogue, the MPI-ESM1-2-LR model exhibits opposite results. In this context, the latter successfully captures the observed historical trend in analogue occurrence, suggesting that it may perform better in representing future trends as well. However, this assumption should be approached with caution. Refer to Sect. 4 for a more detailed discussion of this aspect.

The second most intense heat wave in Europe during 1940–2022 was the one occurred in Scandinavia in 1972, characterized by high HWMId values especially across the northern portion of the region (Fig. 2a). While receiving less attention from the scientific community, this event was comparable in terms of duration and intensity to more widely known heat waves, such as the 2010 Russian and 2003 French heat waves (Table 2). Indeed, the event started on June 26 and lasted about 3 weeks, with HWMId values peaking at approximately 40. The 1972 Scandinavian heat wave was marked by a very persistent high-pressure anomaly over Scandinavia and north-western Russia (Fig. 2b), a region characterized by the highest frequency of summer blocking events in the European continent (Davini and D'Andrea 2020). The atmospheric circulation anomalies featured a large-scale wave-like structure propagating from eastern America to central Siberia, suggesting a role played by the British-Baikal corridor teleconnection along the polar front (Xu et al. 2021). It is also interesting to note that the

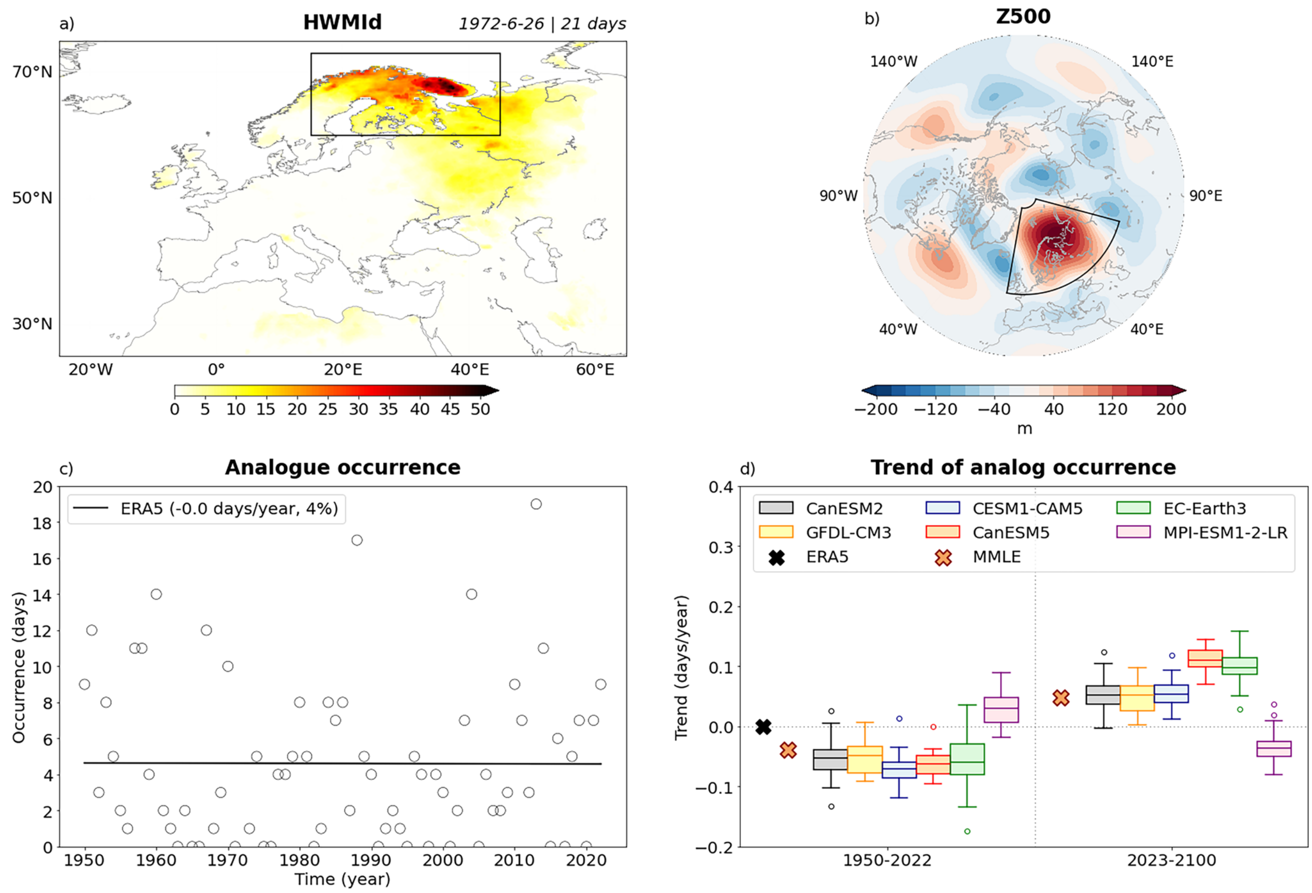

Fig. 2 Same as Fig. 1, but for the 1972 Scandinavian heat wave. In this case, the black box in (**a**) has coordinates 15°E–45°E and 60°N–73°N, while the black box in (**b**) has coordinates 10°W–75°E and 50°N–85°N

atmospheric circulation during the summer 1972 was characterized by a positive and long-lasting phase of the North Atlantic Oscillation (NAO). Please, refer to the daily NAO index as provided by National Oceanic and Atmospheric Administration (link to data available in the Data Availability statement). The summer NAO is an important driver for the development of extreme temperature events in northern Europe (Sinclair et al. 2019; Rousi et al. 2023; Famooss Paolini et al. 2024). Thus, these pieces of evidence suggest that the summer NAO could have also played a role in the 1972 Scandinavian event.

Figure 2 (bottom row) presents analogue trends for 1972 Scandinavian heat wave that are similar to those observed for 2010 Russian heat wave, apart from the historical trend in ERA5. Specifically, no significant trend in the analogue occurrence is evident in the reanalysis for the historical period (Fig. 2c). On the other hand, most models show a general decrease in the analogue occurrence during this period, which is reflected in predominantly negative mean trends, with only a few members showing positive values (Figs. 2d, S2). Furthermore, most models project an increase in the number of days characterized by this analogue in the future across nearly all ensemble members. Despite the future positive trend, the ensemble mean number of analogue days at the end of the twenty-first century remains broadly comparable to that simulated during the historical period, similarly to what shown for the 2010 Russian heat wave (Fig. S2). Once again, the MPI-ESM1-2-LR model generally shows opposing results both for the historical and projection time periods, with only few members aligning with the trends in other models. These aspects highlight a significant uncertainty in the occurrence of the atmospheric analogue associated with 1972 Scandinavian heat wave, similar to what discussed for the 2010 Russian heat wave. In this context, it is worth noting that Yiou et al. (2020) have reported similar results when analysing both observational and model trends of atmospheric analogues for the 2018 Scandinavian heat wave (the ninth event listed in Table 2), which featured an atmospheric circulation pattern remarkably similar to that of the 1972 event.

The third strongest heat wave of past decades was the one that affected central Europe in 2003. The event began on August 3 and lasted approximately 13 days, with the HWMId reaching its maximum values in France, Germany and Northern Italy (Fig. 3a). This event was the culmination of an unusually warm summer, which had already experienced another heat wave in June and exceptionally warm conditions in both May and July (Black et al. 2004). The extreme heat event that struck France in August was partly driven by a persistent atmospheric blocking regime over western Europe (Fig. 3b). The Z500 anomalies were part of a circumglobal wave-like structure, which induced concurrent high temperature anomalies in some regions of North America and Eurasian continent during August (Kornhuber et al. 2019). In this context, it is noted that these anomalies also partially project onto the Eastern Atlantic pattern, which has been shown to be particularly relevant for extreme temperature events in western and central Europe (Cassou et al. 2005; Famooss Paolini et al. 2024). Similarly to the 2010 Russian event, the large amplitudes of the wave-like structures could have been induced by the resonant amplification of quasi-stationary waves due to double jet configuration (Kornhuber et al. 2017). Furthermore, the heat extreme was associated with a Rossby wave packet showing amplitude peak over western Europe (Fragkoulidis et al. 2018).

The occurrence of atmospheric patterns similar to that characterizing the 2003 French heat wave has increased during the historical period. Specifically, ERA5 data indicate an analogue trend of 0.05 days year^{-1}, statistically significant at the 98% confidence level (Fig. 3c). As for the other two heat waves, most models underestimate the observed analogue trend, showing negative model mean and individual members spreading around zero (Fig. 3d). Again, only the MPI-ESM1-2-LR model displays a positive mean trend comparable to observations. In the future, all models project an increase in the occurrence of this atmospheric analogue. In this context, it is noted that, in contrast to the 2010 Russian and 1972 Scandinavian heat waves, models project an increase in the average number of analogue days, despite the negative historical trends (Fig. S3). Thus, the results shown in Fig. 3 suggest that the trend of 2003 French heat wave-like atmospheric circulation patterns is characterized by lower uncertainty compared to other major heat waves occurred in past decades. Jézéquel et al. (2018a) have reached similar conclusions, analysing the dynamic trends of 2003 French and 2010 Russian heat waves in 18 single-member CMIP5 models and one large ensemble. The reduced uncertainty associated with the analogue trend of the 2003 French heat wave is particularly significant, as it enhances the reliability of trend partition analysis, which

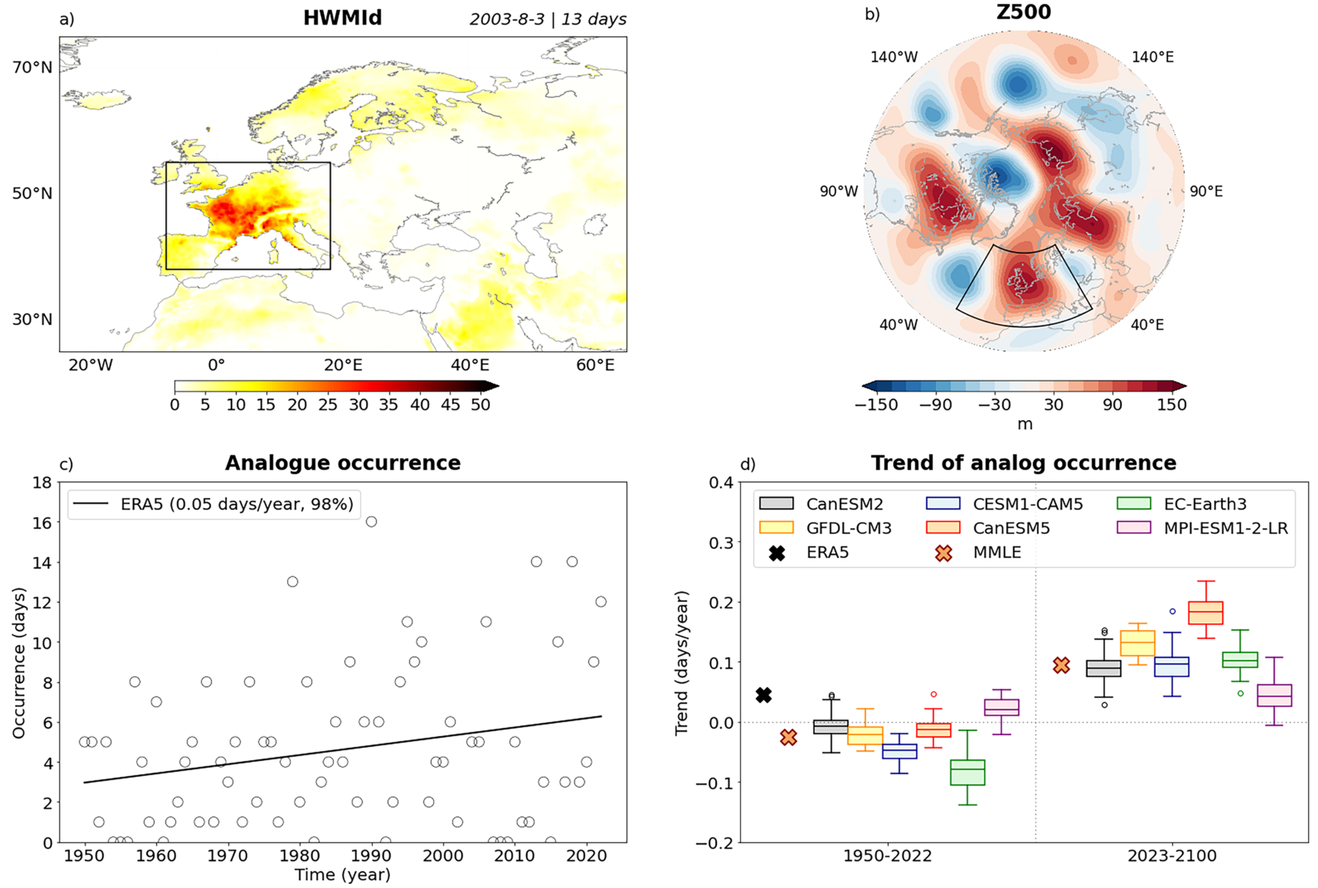

Fig. 3 Same as Fig. 1, but for the 2003 French heat wave. In this case, the black box in (**a**) has coordinates 8°W–18°E and 38°N–55°N, while the black box in (**b**) has coordinates 30°W–30°E and 35°N–65°N

identifies the drivers of historical and future trends in extreme temperature occurrences in western Europe.

As detailed in Sect. 2.3, the atmospheric flow analogue analysis was also performed using larger regions for detecting atmospheric analogues than those illustrated in Figs. 1b–3b. Overall, the results presented in Figs. S4–S6 for all three heat waves are consistent with the findings described above, for both ERA5 and MMLE, and for both the historical and projection periods. More specifically, ERA5 exhibits positive, neutral and positive trends in analogue occurrence during the historical period for the 2010 Russian, 1972 Scandinavian and 2003 French heat wave, respectively. In contrast, the models generally display mean negative trends in the historical period, underestimating the observed analogue trend of the three heat waves. At the same time, the models generally exhibit mean positive trends in the projection period. Once again, the MPI-ESM1-2-LR model consistently diverge from these general patterns, both during the historical and projection periods. It is not completely so for the 2003 French heat wave, as all models exhibit a positive mean trend in the future, with only few members from the MPI-ESM1-2-LR model exhibiting negative values.

Since analogue trends are not significantly affected by the size of the regions used for analogue detection, smaller domains are retained for the analyses presented in subsequent sections. As suggested by Jézéquel et al. (2018b), selecting a tailored domain for flow analogue analysis is optimal as it excludes large-scale features that do not directly impact regional extreme temperatures. Nevertheless, the limited sensitivity of analogue trends to analogue detection region size is consistent with the fact that European extreme temperature events are often associated with large-scale atmospheric structures, characterized by local high-pressure and remote low-pressure systems (Cai et al. 2024; Famooss Paolini et al. 2024).

3.2 Partition of extreme temperature trends

After assessing the dynamic trends of the three most intense heat waves during 1940–2022, we analyse their contributions to historical and projected trends in European extreme temperature occurrences, along with the associated thermodynamic and interaction terms. This analysis is crucial for understanding the mechanisms driving the trends in extreme temperature occurrences and how they may evolve in response to anthropogenic global warming.

Figures 4 and S7 show that the number of extreme temperature occurrences associated with the atmospheric circulation pattern of the 2010 Russian heat wave increased during 1950–2022 in the ERA5 dataset, with a trend of 0.016 days year^{-1} (Table 3). This increase was primarily driven by the thermodynamic and dynamic terms, which account for 75.47 and 58.72% of the total trend, respectively. In contrast, the interaction term offsets these contributions, accounting for − 34.19% of the total trend.

Consistent with observations, all models show a positive historical trend in extreme temperature occurrences, primarily driven by the thermodynamic term. The model mean total trends range from 0.011–0.021 days year^{-1}, with the MMLE mean total trend being 0.014 days year^{-1}. In this context, the thermodynamic term contributes 61.23–109.21% of the total trend across individual models. However, for five out of six models, the dynamic and interaction terms exhibit opposite behavior compared to ERA5, contributing within − 79.87 to − 10.75% and 36.87–71.93% of the total trend, respectively. The opposite contributions of dynamic and interaction terms in the model environment compared to observations reflect the underestimation of observed dynamic component by these models, which is then compensated by a positive contribution from the interaction term. The MPI-ESM1-2-LR model stands out as an exception compared to other models, with its dynamic (interaction) term contributing for about 39.19% (− 0.42%) of the total trend, aligning more closely to observations (Table 3). The thermodynamic, dynamic and interaction terms in the MMLE mean contribute 84.23, − 21.11 and 36.88% of the total trend, respectively.

In the future, all models project a continued increase in the occurrence of extreme temperatures, with future total trends stronger than those observed during the historical period. This indicates that future extreme temperature occurrences will not only become more frequent than in the past but will also increase at a faster rate (Figs. 4, S7). Despite the consistent trend direction, it is interesting to note that the spread of projected total trend values is larger compared to the historical period, reflecting greater internal variability in the future. In this context, the projected mean total trends range within 0.034–0.175 days year^{-1} across individual models, with a MMLE mean of 0.075 days year^{-1}. All trend components exhibit positive values in the future, exceeding those observed in the historical period and contributing to the positive total trend. Specifically, the thermodynamic contribution is projected to account for 20.66–46.36% of the future total trend in single models, thus playing a less relevant role compared to the historical period. Consistently, the difference between the future and historical percentages associated to thermodynamic term are negative (see numbers in parentheses in Table 3). Nonetheless, it is noted that, in the future, nearly all days exhibiting a 2010 Russian heat wave-like atmospheric circulation are projected to coincide with extreme temperatures over western Russia. This is reflected in mean values of h approaching 1 in most models (i.e., close to 100% of analogue days), compared to historical values typically ranging between 0.1 and 0.3 (Fig.

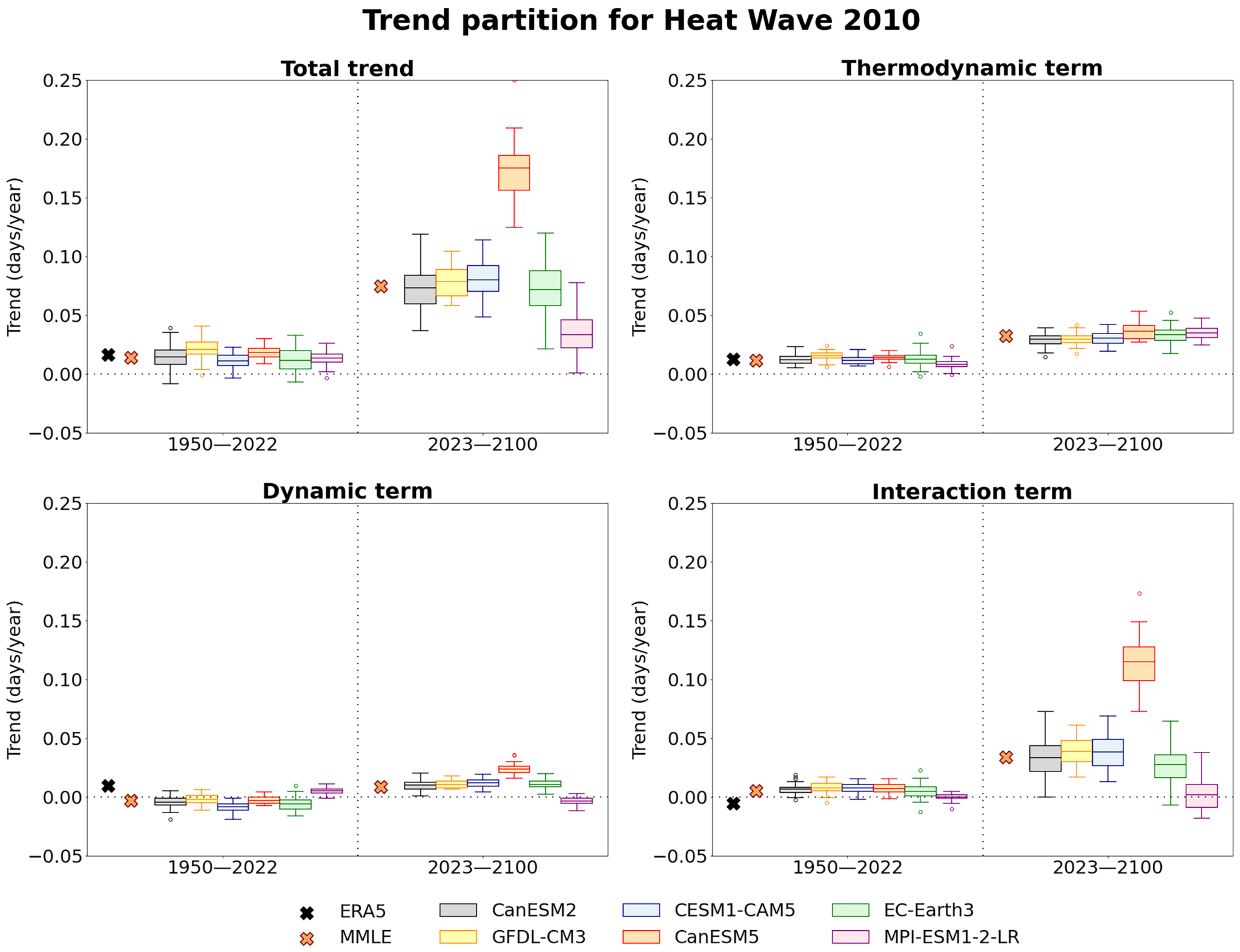

Fig. 4 Partition of the trend (days year^{-1}) in area-weighted extreme temperature days during the occurrence of 2010 Russian heat wave atmospheric analogue. Top left: total trend; top right: thermodynamic term; bottom left: dynamic term; bottom right: interaction term. The number of extreme temperature days is area-weighted averaged in the region with the highest HWMId values during the event (black box, Fig. 1a). Trends are calculated for the historical period (1950–2022) for ERA5 (black cross), the MMLE mean (red cross) and individual models (colored boxplots), and for the projection period (2023–2100) for MMLE mean and individual models. The boxplots display the interquartile range, with the model mean indicated by the horizontal line inside each box. The whiskers extend to 1.5 times the interquartile range, and any outliers beyond this range are shown as individual circles

S10). Meanwhile, the dynamic component will contribute for 13.53–14.91%, becoming more significant in explaining extreme temperature trends than in the past. On the other hand, the interaction component will account for 38.73–65.66% of the total trend. However, no clear conclusions can be drawn about the changes in its relative importance, as half the models indicate a greater importance, while the other half suggests the opposite. In this context, we note that the interaction term is associated with the largest spread due to significant internal variability and inter-model differences, which mostly explains the wide spread of the projected total trends. Yet again, the MPI-ESM-LR model shows different results, with the thermodynamic, dynamic and interaction term contributing 104.08, − 59.26 and − 29.01% to the mean total trend. Thus, these findings suggest that, for this model, the thermodynamic term will play a more significant role compared to the past, whereas the dynamic and interaction terms will become less important. Taking into account all the models, results shows that the thermodynamic, dynamic and interaction terms will contribute 43.05, 11.82 and 45.13% of the total trend, respectively.

Consistent with the results shown in Sect. 3.1, the trend partition analysis for the 2010 Russian heat wave is marked by significant uncertainty due to inter-model spread and internal climate variability. This is particularly true for the dynamic and interaction terms, as models exhibit different future changes compared to the past. This uncertainty prevents to draw definitive conclusions about the mechanisms that will drive extreme temperature trends in western Russian.

Table 3 Partition of the trend (days year^{-1}) in area-weighted extreme temperature days during the occurrence of 2010 Russian heat wave atmospheric analogue

	1950–2022				2023–2100			
	Total trend (days year^{-1})	Thermodynamic term (%)	Dynamic term (%)	Interaction term (%)	Total trend (days year^{-1})	Thermodynamic term (%)	Dynamic term (%)	Interaction term (%)
ERA5	0.016	75.47	58.72	− 34.19	–	–	–	–
CanESM2	0.014	83.73	− 30.15	46.42	0.073	40.27 (− 43.46)	13.82 (43.97)	45.91 (− 0.51)
GFDL-CM3	0.021	73.88	− 10.75	36.87	0.079	37.39 (− 36.49)	13.53 (24.28)	49.08 (12.21)
CESM1-CAM5	0.011	107.94	− 79.87	71.93	0.080	37.71 (− 70.23)	14.79 (94.66)	47.50 (− 24.43)
CanESM5	0.018	74.82	− 15.05	40.22	0.175	20.66 (− 54.16)	13.68 (28.73)	65.66 (25.44)
EC-Earth3	0.011	109.21	− 51.95	42.74	0.071	46.36 (− 62.85)	14.91 (66.86)	38.73 (− 4.01)
MPI-ESM1-2-LR	0.013	61.23	39.19	− 0.42	0.034	104.08 (42.85)	− 9.88 (− 49.07)	5.81 (6.23)
MMLE	0.014	84.23	− 21.11	36.88	0.075	43.05 (− 41.18)	11.82 (32.92)	45.13 (8.26)

The number of extreme temperature days is area-weighted averaged in the region with the highest HWMId values during the event (black box, Fig. 1a). The thermodynamic, dynamic and interaction terms are expressed as percentages of the total trend for the model and MMLE mean. Differences between the future and historical percentages for each component are shown in parentheses below the future trend values

Figure 5 presents the trend partition analysis for extreme temperature occurrences associated with atmospheric circulation similar to 1972 Scandinavian heat wave. Similarly to the 2010 Russian heat wave, the reanalysis dataset shows an increase in the number of extreme temperature occurrences over the historical period, with a trend of 0.011 days year^{-1} (Table 4). However, in this case the total trend was primarily driven by the interaction term (80.54%), while thermodynamic (21.01%) and dynamic (− 1.55%) components play secondary role (Table 4).

Model historical trends are marked by large internal variability and model spread. Indeed, most models exhibit positive mean total trend within the range 0.003–0.02 days year^{-1}, with individual member values fluctuating around zero, while CESM1-CAM5 CMPI5 model shows an average reduction in extreme temperature occurrences. Nonetheless, in agreement with observations, the MMLE mean shows a trend that is largely driven by thermodynamic (164.86%) and interaction (97.02%) terms, with the dynamic component acting in opposition (− 161.88%). A similar trend partition is observed in four out of six models, with these terms accounting for 57.34–333.33%, − 422.05 to − 49.84% and 67.60–238.21% of the total trend, respectively. Differently, the CESM1-CAM5 and MPI-ESM1-2-LR models are an exception. Indeed, the CESM1-CAM5 model exhibits thermodynamic, dynamic and interaction terms that are similar in amplitude and sign to those of other models; however, due to its negative total trend, the relative contributions of these terms are reversed. On the other hand, MPI-ESM1-2-LR model exhibits a positive contribution from dynamic component, consistent with the analogue trend in Fig. 2d. It is specified that the model percentages shown in Table 4 can reach particularly high values due to the small total trend, which serves as the denominator in the percentage calculation.

In future projections, all models display an overall increase in the occurrence of extreme temperature days associated with the 1972 Scandinavian analogue relative to the historical period (Fig. S8), with positive mean total trends ranging within 0.011–0.125 days year^{-1}, and a MMLE mean trend of 0.066 days year^{-1}. This is not true for a few model members from the MPI-ESM-LR models, which show a reduction in extreme temperature occurrences. For most models, all trend components are expected to contribute to the total trend. Table 4 indicates that the future thermodynamic and interaction components will play a less significant role compared to the historical period, contributing 22.75–43.57% and 33.69–56.86%, respectively, across individual models, and 40.48 and 41.77% in the MMLE mean. Conversely, the dynamic component will become more important accounting for 14.37–22.74% of the total trend across individual models and for 17.75% in the MMLE. Nonetheless, intermodel differences still emerge, with MPI-ESM-LR models showing opposite results. Indeed, its mean dynamic and interaction terms will be negative in the future, with the former becoming less relevant in explaining the total trend compared to the past. In this case, the thermodynamic term will primarily account for the future total trend, becoming more relevant compared to the past. Apart from these intermodel differences, all models simulate a large portion of future analogue days coinciding with extreme temperatures over the Scandinavia (Fig. S11). In several cases, individual

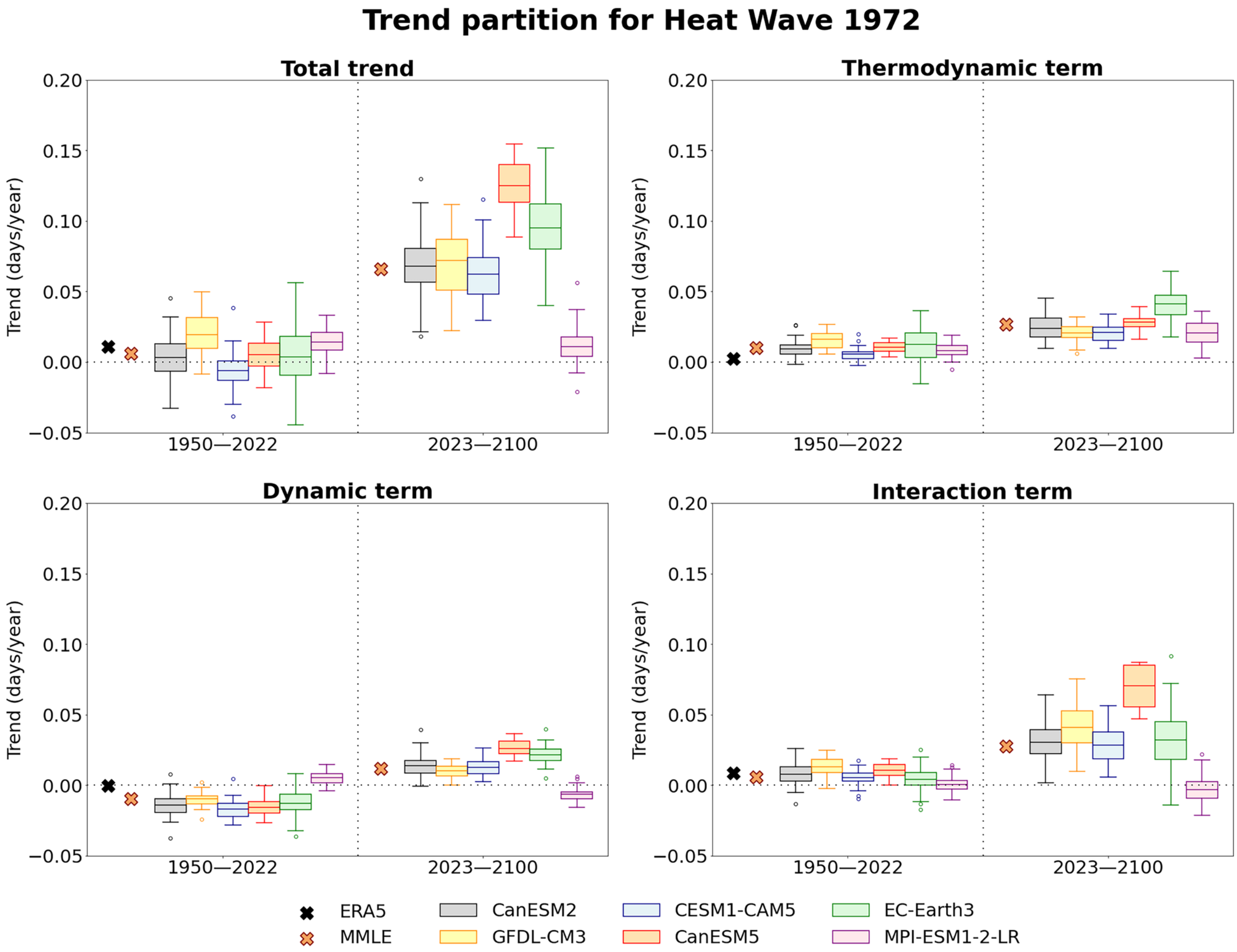

Fig. 5 Same as Fig. 4, but for the 1972 Scandinavian heat wave. In this case, the number of extreme temperature days is area-weighted averaged in the black box shown in Fig. 2a

Table 4 As Table 3, but for the 1972 Scandinavian heat wave. In this case, the number of extreme temperature days is area-weighted averaged in the black box shown in Fig. 2a

	1950–2022				2023–2100			
	Total trend (days year^{-1})	Thermodynamic term (%)	Dynamic term (%)	Interaction term (%)	Total trend (days year^{-1})	Thermodynamic term (%)	Dynamic term (%)	Interaction term (%)
ERA5	0.011	21.01	− 1.55	80.54	–	–	–	–
CanESM2	0.003	283.83	− 422.05	238.21	0.068	34.79 (− 249.04)	20.56 (442.60)	44.65 (− 193.56)
GFDL-CM3	0.020	82.24	− 49.84	67.60	0.072	28.77 (− 53.47)	14.37 (64.21)	56.86 (− 10.73)
CESM1-CAM5	− 0.006	− 92.16	281.48	− 89.32	0.062	33.60 (125.76)	20.50 (− 260.98)	45.89 (135.22)
CanESM5	0.005	192.14	− 291.96	199.82	0.125	22.75 (− 169.38)	20.87 (312.82)	56.38 (− 143.44)
EC-Earth3	0.004	333.33	− 347.64	114.31	0.095	43.57 (− 289.76)	22.74 (370.38)	33.69 (− 80.62)
MPI-ESM1-2-LR	0.014	57.34	37.85	4.81	0.011	188.27 (130.93)	− 59.26 (− 97.12)	− 29.01 (− 33.82)
MMLE	0.006	164.86	− 161.88	97.02	0.066	40.48 (− 124.38)	17.75 (179.63)	41.77 (− 55.25)

model members reach *h* equal to 1 already at the beginning of the projection period. This behaviour emerges earlier and more systematically than in the 2010 Russian case, and is consistent with the Arctic amplification, whereby the Arctic and high latitudes warm more and faster than lower latitudes (Serreze and Barry 2011).

Similarly to the 2010 Russian heat wave and consistent with the analogue trends shown in Fig. 2, the trend partition results for the 1972 Scandinavian heat wave are also subjected to a certain degree of uncertainty. This uncertainty diminishes confidence in projections of future changes in the drivers of extreme temperature occurrences linked to these analogues.

Finally, we analyse the trend components for extreme temperature occurrences associated with the atmospheric pattern of the 2003 French heat wave. Figures 6 and S9 show an increase in the number of extreme temperature days over the historical period in ERA5 dataset, with a trend of 0.022 days year^{-1} (Table 5). Similar to results associated with 2010 Russian heat wave, the trend was mainly driven by the thermodynamic (83.63%) and dynamic (30.19%) components, while the interaction term partially offsets these contributions (− 13.82%).

In agreement with ERA5, models show positive total trends, with mean values in the range 0.003–0.016 days year^{-1} and a MMLE mean of 0.012 days year^{-1}. These trends are driven by a strong thermodynamic component, accounting for 100.76% of the total trend in the MMLE mean and for 67.04–374.45% across individual models. However, in contrast to ERA5, the models show a negative contribution from the dynamic term (− 29.41) and a positive contribution from the interaction term (28.66%) in the MMLE mean. This is so also for five out of six models, with the dynamic contribution ranging within − 300.05 to − 7.50% and the interaction contribution within 22.38–58.77%. Notably, the MPI-ESM1-2-LR model stands out as an exception, with the dynamic term contributing positively to the total trend (20.55%), similar to the observations.

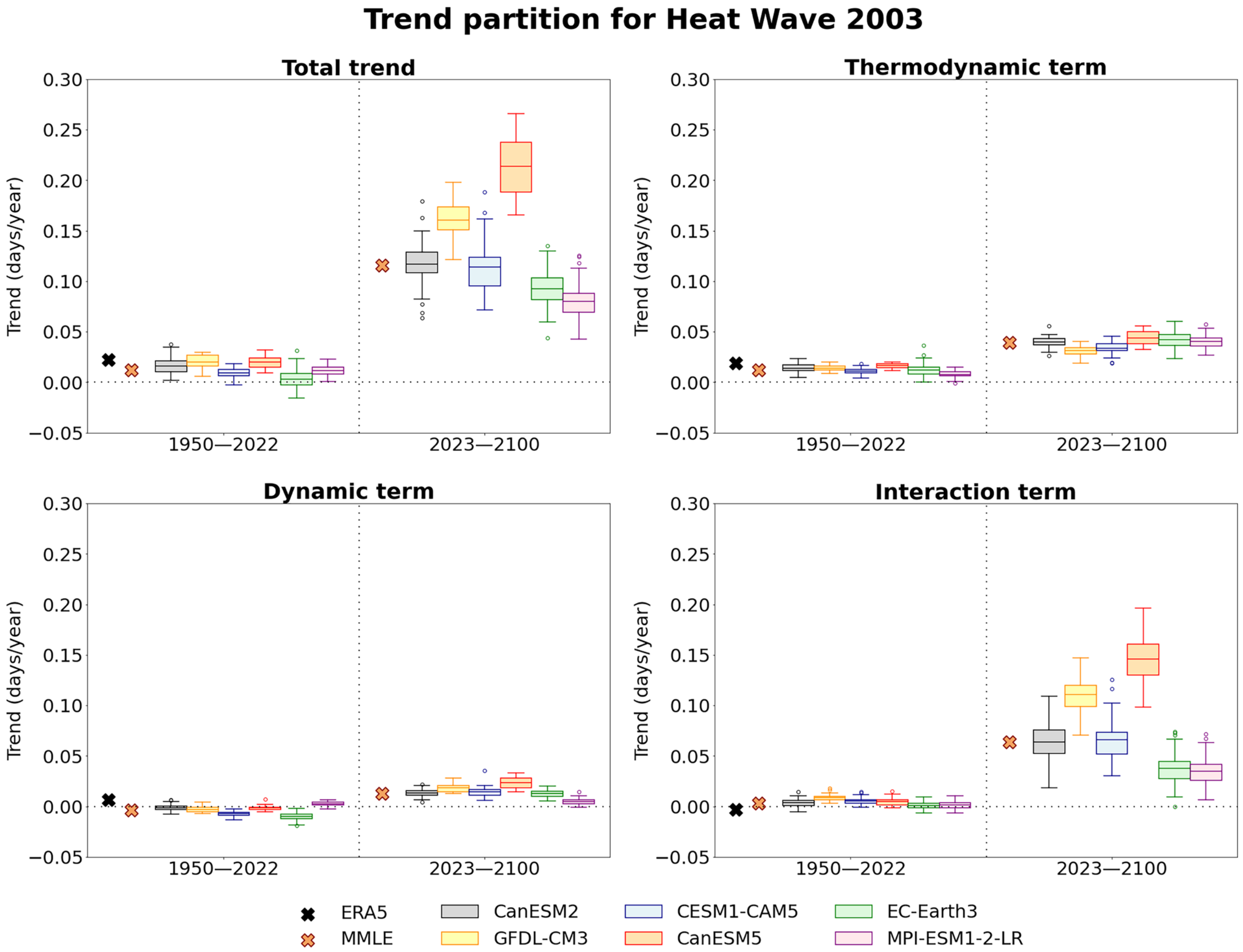

Fig. 6 Same as Fig. 4, but for the 2003 French heat wave. In this case, the number of extreme temperature days is area-weighted averaged in the black box shown in Fig. 3a

Table 5 As Table 3, but for the 2003 French heat wave. In this case, the number of extreme temperature days is area-weighted averaged in the black box shown in Fig. 3a

	1950–2022				2023–2100			
	Total trend (days year^{-1})	Thermodynamic term (%)	Dynamic term (%)	Interaction term (%)	Total trend (days year^{-1})	Thermodynamic term (%)	Dynamic term (%)	Interaction term (%)
ERA5	0.022	83.63	30.19	− 13.82	–	–	–	–
CanESM2	0.016	85.12	− 7.50	22.38	0.117	34.12 (− 51.00)	11.52 (19.02)	54.36 (31.99)
GFDL-CM3	0.020	69.31	− 14.03	44.72	0.161	19.48 (− 49.83)	11.44 (25.47)	69.08 (24.36)
CESM1-CAM5	0.009	121.56	− 80.32	58.77	0.114	29.43 (− 92.12)	12.69 (93.02)	57.97 (− 0.89)
CanESM5	0.020	83.11	− 8.13	25.02	0.214	20.56 (− 62.55)	11.08 (19.21)	68.36 (43.34)
EC-Earth3	0.003	374.45	− 300.05	25.60	0.092	45.51 (− 328.94)	13.66 (313.71)	40.83 (15.23)
MPI-ESM1-2-LR	0.012	67.04	20.55	12.40	0.080	50.22 (− 16.82)	5.96 (− 14.59)	43.81 (31.41)
MMLE	0.012	100.76	− 29.41	28.66	0.116	33.81 (− 66.95)	11.16 (40.57)	55.03 (26.38)

In the future, results are characterized by a smaller uncertainty compared to the other heat waves here analysed. Indeed, all models project an increase in the extreme temperature occurrences (Fig. S9), with future total trends stronger than those during the historical period (Fig. 6). These projected trends range within 0.08–0.214 days year^{-1}, with a MMLE mean of 0.116 days year^{-1}. Additionally, all trend components are expected to be positive in the future, contributing to the overall trend, both in the model mean and single model members. This consistency reduces the uncertainty in future changes compared to historical period caused by internal variability and inter-model differences. As for the other heat waves, the relative contributions of trend components to the total trend are expected to change. Specifically, similar to the 2010 Russian heat wave, the thermodynamic contribution is projected to play a less relevant role compared to the historical period. Yet, consistent with other heat waves, the results show that the fraction of days with 2003 French heat wave-like circulation that also exhibit extreme temperatures (h) will increase markedly compared to the past (Fig. S12). On the other hand, the dynamic and interaction terms are expected to become more significant compared to the past. The thermodynamic, dynamic and interaction terms will account for 33.81% (19.48–50.22%), 11.16% (5.96–13.66%) and 55.03% (40.83–69.08%) of the total trend in the MMLE (individual model) mean. Notably, the MPI-ESM1-2-LR model also exhibits a positive contribution of the future dynamic trend, though smaller than the historical period, resulting in a negative percentage difference in Table 5.

3.3 Decomposition of the interaction term and land–atmosphere coupling

Results in previous section indicate that the interaction term is projected to increase in the future, largely explaining the overall future rise in extreme temperature occurrences associated with the atmospheric analogues of the three major heat waves during 1940–2022. Since previous studies have linked this term to processes potentially involving the land–atmosphere coupling (Horton et al. 2015; Rogers et al. 2022), these results may suggest a crucial role of coupling mechanisms in explaining future projection of extreme temperature occurrences. However, as suggested by other studies (Sui et al. 2020), the physical interpretation of the interaction term should be considered with caution. As clarified in Sect. 2.5, changes in this term may arise not only from changes in the year-to-year covariance between thermodynamic and dynamic conditions, but also from their co-evolving long-term trends. Given the pronounced trends in f and h shown in Figs. S1–S3 and S10–S12, this possibility can not be excluded here. We therefore decompose this term as explained in Sect. 2.5 to assess how much of its contribution is related to changes in the mean state of f' and h' and how much instead arises from changes in their effective covariability. We focus on the 2003 French heat wave, for which results in previous section are characterized by comparatively small uncertainties due to internal variability and inter-model differences than the 2010 Russian and 1972 Scandinavian heat waves.

Figure 7 and Table 6 indicate that the interaction term reflects multiple sources of change, and should therefore not be interpreted uncritically as a measure of pure covariability between thermodynamic and dynamic conditions. As discussed in the previous section, the full interaction term over 1950–2022 is small in ERA5 and in most models. In ERA5, this signal mainly arises from comparable contributions of the trend–trend component and from the detrended covariance term, partly compensated by the two mixed components. In the MMLE and in most individual models, the largest contribution typically arises from the detrended covariance term. By contrast, the interaction term becomes substantially larger in the projection period and is almost entirely dominated by the trend–trend component, consistent with the strong long-term increases in both *f* (Fig. S3) and *h* (Fig. S12). For the MMLE and most individual models, this term alone explains nearly 100 % of the full interaction term, while the remaining three contributions each account for only a few percent and often compensate one another (Table 6).

Although the detrended covariance term explains only a portion of the interaction term, the results above do not exclude that it may still reflect land–atmosphere coupling processes. To further investigate the physical meaning of the interaction term, we relate the $h'_d \cdot f'_d$ product to a land–atmosphere coupling diagnostic as described in Sect. 2.5. Figure 8 shows that the $h'_d \cdot f'_d$ product is generally positive in both ERA5 and the models, indicating that the detrended thermodynamic and dynamic anomalies tend to covary in the same direction. If h'_d and f'_d were largely independent, their product would be expected to fluctuate more symmetrically around zero. In addition, consistent with the positive land–atmosphere feedback proposed by Koster et al. (2016), Figure 8 also shows an overall positive SHF–analogue correlation, and a systematic relationship between its intensity and the $h'_d \cdot f'_d$ product in both the historical and projection periods. Specifically, larger values of $h'_d \cdot f'_d$ product tend to be associated with stronger SHF–analogue correlations. However, only a limited fraction of $h'_d \cdot f'_d$ variance is explained by the linear relationship with the coupling intensity, as shown by the small coefficient of determination (R^2) both during the historical and projection periods. Furthermore, it is noted that the mean correlation values appear weak both in ERA5 and model ensemble (around 0.2), largely reflecting large internal variability. Indeed, some 30-year windows are characterized by relatively strong positive correlations while others exhibit near-zero or even opposite values. As a result, similar values of $h'_d \cdot f'_d$ can be associated with markedly different coupling estimates.

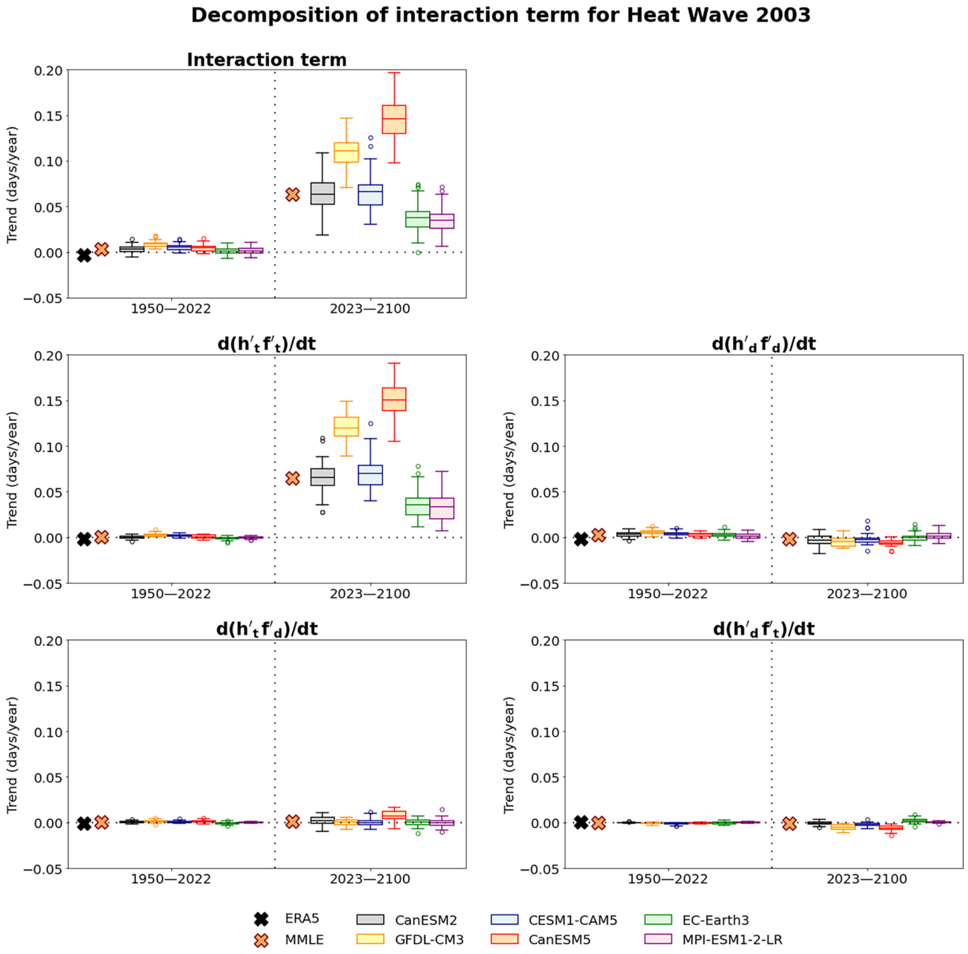

Fig. 7 Decomposition of the interaction term (days year^{-1}) for the 2003 French heat wave. Top left: interaction term; central left: $\frac{d(h'_t f'_t)}{dt}$; central right: $\frac{d(h'_d f'_d)}{dt}$; bottom left: $\frac{d(h'_t f'_d)}{dt}$; bottom right: $\frac{d(h'_d f'_t)}{dt}$. Trends are calculated for the historical period (1950–2022) for ERA5 (black cross), the MMLE mean (red cross) and individual models (colored boxplots), and for the projection period (2023–2100) for MMLE mean and individual models. The boxplots display the interquartile range, with the model mean indicated by the horizontal line inside each box. The whiskers extend to 1.5 times the interquartile range, and any outliers beyond this range are shown as individual circles

Table 6 Decomposition of the interaction term (days year^{-1}) for the 2003 French heat wave. Columns report the full interaction term and its four components, $\frac{d(h'_t f'_t)}{dt}$, $\frac{d(h'_d f'_d)}{dt}$, $\frac{d(h'_t f'_d)}{dt}$, and $\frac{d(h'_d f'_t)}{dt}$, for both the historical and projection periods. For each model and the MMLE, the single components are expressed as percentages of the corresponding ensemble mean interaction term

	1950–2022					2023–2100				
	Interaction term (days year^{-1})	$\frac{d(h'_t f'_t)}{dt}$ (%)	$\frac{d(h'_d f'_d)}{dt}$ (%)	$\frac{d(h'_t f'_d)}{dt}$ (%)	$\frac{d(h'_d f'_t)}{dt}$ (%)	Interaction term (days year^{-1})	$\frac{d(h'_t f'_t)}{dt}$ (%)	$\frac{d(h'_d f'_d)}{dt}$ (%)	$\frac{d(h'_t f'_d)}{dt}$ (%)	$\frac{d(h'_d f'_t)}{dt}$ (%)
ERA5	− 0.003	60.34	54.01	16.16	− 30.51	–	–	–	–	–
CanESM2	0.004	2.43	88.83	10.38	− 1.64	0.064	102.70	− 4.81	3.15	− 1.04
GFDL-CM3	0.009	31.43	64.66	13.43	− 9.52	0.111	107.91	− 3.86	0.50	4.55
CESM1-CAM5	0.005	35.31	73.92	13.50	− 22.72	0.066	106.03	− 3.10	0.30	− 3.23
CanESM5	0.005	14.88	65.81	28.15	− 8.85	0.146	103.04	− 4.06	5.09	− 4.07
EC-Earth3	0.001	− 121.21	334.91	− 64.50	− 49.20	0.038	94.07	− 0.97	0.74	6.15
MPI-ESM1-2-LR	0.001	− 17.99	95.17	6.63	16.19	0.035	94.82	4.58	− 0.51	1.11
MMLE	0.003	10.46	90.47	9.74	− 10.67	0.064	102.02	− 2.57	1.90	− 1.35

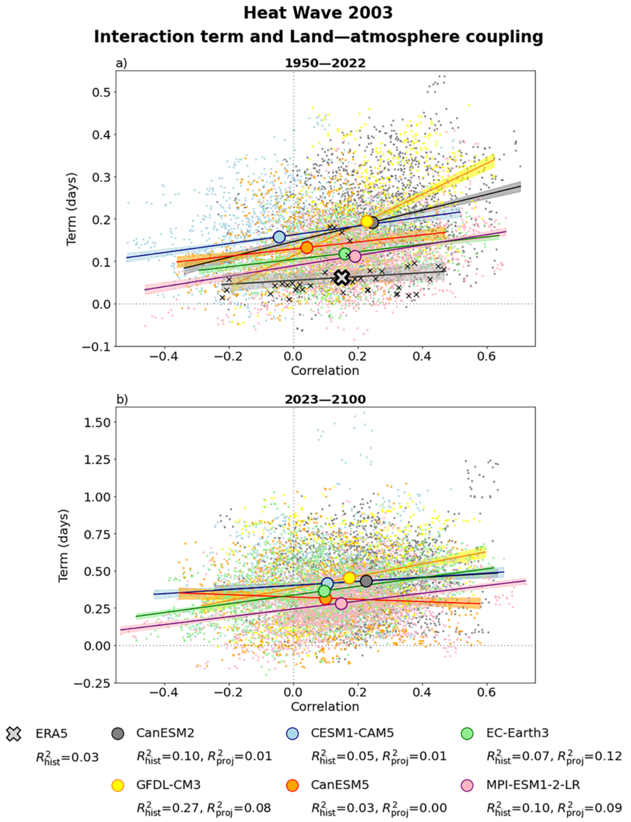

Fig. 8 **a** Scatterplot relating the $h'_d \cdot f'_d$ product (days^{-1}) to land–atmosphere coupling during the historical period (1950–2022) for the 2003 French heat wave. The land–atmosphere coupling is assessed through the correlation between the summer SHF and analogue occurrence using a 30-year running window, and is paired with the mean value of the $h'_d \cdot f'_d$ product over the same window. Results are shown for individual model members during each 30-year window (small circles) and for model means (large circles). Solid lines denote the least squares regression between the correlation and the $h'_d \cdot f'_d$ product. Shaded areas indicate the 95% confidence interval of the regression, based on a bootstrap test performed 1000 times. The coefficient of determination (R^2) is reported in the legend for each dataset as a measure of the fraction of $h'_d \cdot f'_d$ variance explained by the land–atmosphere coupling. **b** Same as (**a**), but for the projection period (2023–2100)

Overall, results presented in this section suggest that the interaction term may capture aspects of land–atmosphere coupling, but this interpretation should be taken with caution, partly in agreement with Sui et al. (2020). Indeed, a fraction of the interaction term reflects the long-term trends in its thermodynamic and dynamic components, which are not necessarily causally linked through coupling processes. In addition, the coupling diagnostic used here remains highly sensitive to internal variability and explains only a limited fraction of $h'_d \cdot f'_d$ variance. Thus, the methodological framework adopted here does not allow us to draw definitive conclusions on the contribution of land–atmosphere coupling to trends in extreme temperature occurrences. A consistent picture emerges for the 2010 Russian and 1972 Scandinavian heatwaves, both for the interaction term decomposition (Figs. S13–S14, Tables S1–S2) and for its relationship with land–atmosphere coupling (Figs. S15–S16). Refer to Sect. 4 for further discussion about the results presented above.

4 Discussion

The results presented in previous section should be interpreted with caution due to uncertainties primarily arising from inter-model differences. This is particularly true for the 2010 Russian (Figs. 1, 4, S1, S4 and Table 3) and 1972 Scandinavian heat waves (Figs. 2, 5, S2, S5 and Table 4), as models do not provide consistent future projections of their dynamic trends. A common approach to reduce model uncertainty in future climate projections is to constrain the latter using observed historical data (e.g., Vogel et al. 2018; Hegerl et al. 2021). This approach relies on the assumption that models better representing historical climate will also perform better in the future. Since atmospheric dynamics is a central aspect of the present work, one potential way to enhance the reliability of atmospheric flow analogue and partition trend analyses could be to select only those models that closely reproduce observed historical analogue trends. This choice is also justified by the fact that most models analysed here tend to underestimate the historical dynamic trends associated with the 2010 Russian, 1972 Scandinavian and 2003 French heat waves. The model underestimation of dynamic trends is in agreement with and partly extends the study by Vautard et al. (2023), who reported that state-of-the-art CMIP6 models underestimate the trend in daily maximum temperatures driven by dynamic changes over western Europe during 1950–2022. In the context of the present work, the MPI-ESM1-2-LR model would be predominantly selected for the constrained climate projections, being the model that better represents the historical dynamic trends. As a result, we could expect a reduction in atmospheric analogue occurrences for the 2010 Russian and 1972 Scandinavian heat waves, alongside future increases in extreme temperature occurrences primarily driven by thermodynamic component and counteracted by dynamic term (Tables 3–4, line 7). However, the assumption that models accurately representing observed historical climate will necessarily perform better in future projections has been shown to not be always valid (Knutti et al. 2010). Moreover, we point out that the ERA5 historical dynamic trend falls within the inter-model spread and is also captured by members of models other than MPI-ESM1-2-LR model, which exhibit different behaviors during the projection period compared to the latter. Finally, some members of MPI-ESM1-2-LR model exhibit positive future trends similar to those of other models. All these aspects complicate efforts to draw definitive conclusions about dynamic trends and trend partitions for the 2010 Russian and 1972 Scandinavian two heat waves. As stated by previous studies (e.g., Vautard et al. 2023), the results presented here provide additional evidence underscoring the importance of directing future research efforts toward identifying the sources of model biases in representing the atmospheric circulation dynamics and variability during historical period. Addressing these biases is essential for improving our comprehension of climate extremes and their future changes.

Results for the 2003 French extreme event are subject to lower uncertainty compared to the other two heat waves. While the inter-model spread in future analogue trend remains considerable, all models consistently project an increase in future atmospheric analogue frequency (Figs. 3, S3 and S6), thus providing a greater reliability on trend partition analysis (Fig. 6, Table 5). In this context, the application of constraining methodology may narrow the range of future values and potentially change the relative contributions of single terms on the total trend within trend partition analysis. However, this would not alter the sign of the projected changes, nor would affect the key conclusions of the analyses conducted for the 2003 French heat wave.

Given the lower uncertainties in the results, we discuss here the potential drivers behind the projected increase in atmospheric circulation patterns resembling that of the 2003 French heat wave. Arctic amplification has been shown to weaken the geopotential gradient between high and low latitudes, reducing the extra-tropical zonal flow and resulting in a more meandering jet stream (Francis and Vavrus 2012). This, in turn, may result in Rossby waves with larger amplitudes and smaller phase velocity, potentially increasing the persistence and frequency of positive geopotential height anomalies over western Europe (Kornhuber et al. 2019). Moreover, Arctic amplification has been linked to an enhanced Arctic front jet due to the increased land–sea thermal contrast at high latitudes (Coumou et al. 2018). This process promotes a higher frequency of double jet configurations over the Eurasian continent, which could lead to more favorable conditions for resonance of free and forced synoptic waves (Petoukhov et al. 2013; Mann et al. 2017; Rousi et al. 2022). Consequently, the amplitude and frequency of wave ridges at mid-latitudes may be increased, further amplifying summer extreme temperatures (Kornhuber et al. 2017). The increasing frequency of atmospheric analogues associated with 2003 French heat wave could be also linked to changes in Rossby wave sources and teleconnections. Several studies have highlighted the relevance of tropical convection, oceanic conditions, and land surface processes in generating phase-locked Rossby wave trains that propagate across the Northern Hemisphere (Cassou et al. 2005; Teng et al. 2019; Wang et al. 2019; Beverley et al. 2021). In this context, global warming has been associated with changes in the position of the intertropical convergence zone (Weller et al. 2014; Mamalakis et al. 2021), soil moisture drying in North America and central Europe (Seneviratne et al. 2006; Overpeck and Udall 2020), and the intensification of Indian monsoon rainfall and variability (Katzenberger et al. 2020). Being all these processes key for the Rossby waves generation and propagation, climate change may also be related with higher frequency in specific atmospheric circulation patterns through its effect on Rossby wave activity and their preferred phase position over western Europe. Finally, over longer timescales, the increased frequency of blocking-type atmospheric circulation over western Europe may be linked to the Atlantic warming hole–a region in the extratropical North Atlantic exhibiting a cooling trend in sea surface temperature, partly attributed to the weakening of the Atlantic Meridional Overturning Circulation (Drijfhout et al. 2012). Given that several past extreme temperature events in western Europe have been associated with negative sea surface temperature anomalies in the same region (Duchez et al. 2016), the Atlantic warming hole could further amplify the occurrence of the atmospheric analogues associated with the 2003 French heat wave.

Despite the uncertainties in the dynamic trend mentioned at the beginning of this section, the partition trend analysis generally indicates a future enhancement of the interaction term (Figs. 4–6, Tables 3–5). Because this term has been suggested to capture land–atmosphere coupling processes (e.g., Horton et al. 2015), its projected increase may imply a growing influence of coupling mechanisms on future rise of extreme temperature occurrences. However, partly in line with the concerns raised by Sui et al. (2020), our results indicate that the physical interpretation of the interaction term should be taken with caution. First, we do find a relationship between the interaction term and coupling intensity, with larger values of the $h'_d \cdot f'_d$ product generally associated with stronger coupling (Figs. 8, S15, S16). Yet, the interaction term decomposition shows that the contribution most directly related to thermodynamic–dynamic covariability ($\frac{d(h'_d f'_d)}{dt}$) accounts for only a fraction of the full interaction term, particularly in the projection period (Figs. 7, S13, S14; Tables 6, S1, S2). Moreover, the SHF–analogue correlation is strongly modulated by internal variability and explains only a limited portion of the thermodynamic–dynamic covariability (Figs. 8, S15, S16). Thus, these results imply that the future increase in the extreme temperature events analysed here is largely driven by the concurrent long-term changes in thermodynamic and dynamic components composing the interaction term, rather than unambiguous changes in the land–atmosphere coupling measured by our diagnostic.

At the same time, it should be considered that the interaction term may still reflect aspects of land–atmosphere coupling not explicitly represented by the diagnostic adopted here (Teuling et al. 2010; Li et al. 2021), and that other large-scale drivers may modulate summer temperature trends across Europe. For instance, European summer temperatures have been linked to the Atlantic multidecadal variability (Sun et al. 2015; Ehsan et al. 2020; Nicolì et al. 2020) as well as to the Arctic sea-ice extent and variability through local feedbacks (Ruggieri et al. 2017; Delhaye et al. 2021). Such influences may contribute to explain the interaction term, potentially masking the role of land–atmosphere coupling in driving extreme temperature trends. In addition, the relationship between the interaction term and land–atmosphere coupling may be sensitive to the methodological choices made in this study. For example, the strategy to define detrended thermodynamic (h'_d), dynamic (f'_d), and SHF anomalies, as well as the assumed linearity of the fitted relationship, could all affect the results. In this context, it is also worth noting that recent evidence indicates land–atmosphere coupling can vary substantially across extreme temperature events affecting the same region, and can be spatially heterogeneous within a given event (Yoon et al. 2026; e.g., during the 2010 Russian and 2003 French heat waves). This suggests that using seasonal and spatially-average data to assess land–atmosphere coupling may mix areas and periods characterized by distinct coupling regimes, potentially explaining the large spread in coupling diagnostic found here and its weak relationship with the thermodynamic–dynamic covariability term. More detailed analyses are required to fully disentangle the land–atmosphere coupling and its implications for trends in extreme temperature occurrences, as well as to better understand the physical processes most strongly reflected by the interaction term.

5 Conclusions

Numerous studies have linked the rise in summer extreme temperature frequency across Europe to a combination of atmospheric and thermodynamic changes, as well as their mutual interaction (e.g., Horton et al. 2015; Seneviratne et al. 2010). However, the role of atmospheric dynamic changes remains debated, and a comprehensive analysis of the mechanisms underlying the extreme temperature trends is still lacking.

The present study addresses these gaps by analyzing historical and future trends in the occurrence of atmospheric analogues associated with three of the most intense heat waves in past decades: the 2010 Russian, 1972 Scandinavian and 2003 French heat waves. These heat waves are here identified as the strongest during 1940–2022 through the HWMId as defined by Russo et al. (2015). Then, we decompose the associated trends of summer extreme temperature occurrences into their thermodynamic, dynamic and interaction terms. The analyses are performed using ERA5 reanalysis and a MMLE dataset composed of 6 models, each providing between 20 and 50 members and under the "business-as-usual" emission scenario for future projections. This allows us to assess the role of the global warming, internal climate variability and model spread on trends of European extreme temperature occurrences.

In agreement with previous studies (e.g., Horton et al. 2015), results show that the frequency of atmospheric analogues associated with the 2003 French heat wave has increased during 1950–2022 in ERA5 (Figs. 3c, S3), explaining about one-third of the historical rise in extreme temperature occurrences linked to these analogues (Fig. 6, Table 5). The remaining portion of the trend in extreme temperature occurrences is explained by the thermodynamic component, which emerges as the most significant contributor, while the interaction term acts in opposition. The MMLE reproduces the overall increase in extreme temperature occurrences associated with these analogues but not the observed partition, with the dynamic and interaction terms exhibiting opposite behavior compared to observations (Fig. 6, Table 5). This discrepancy reflects the model underestimation of historical analogue trend, with most models showing negative ensemble mean trend values and individual members fluctuating around zero (Fig. 3d). Among the models, MPI-ESM1-2-LR model performs the best in reproducing the historical analogue trend, exhibiting a partition of the trend in extreme temperature occurrences that aligns more closely with observations.

In future projections, models consistently project an increase in the frequency of atmospheric analogues for the 2003 French heat wave. This increase will account for about one-tenth of the future trend in extreme temperature occurrences, with the interaction term emerging as the primary contributor, followed by the thermodynamic component. Accordingly, the partition trend analysis indicates that dynamic and interaction contributions will become more significant in the future, while the thermodynamic component influence will decrease (percentage differences in Table 5). However, caution is warranted due to the underestimation of historical analogue trends, which affects the contribution of dynamic and interaction terms in the historical period and, thus, the eventual changes of their percentage contribution in the future.

The results for the 2010 Russian and 1972 Scandinavian heat waves exhibit greater uncertainty compared to the 2003 French event due to inter-model differences and internal climate variability, impacting the reliability of future projections for analogue frequency and the mechanisms driving extreme temperature trends in these European regions. ERA5 data indicate an increasing historical trend in atmospheric analogues for the 2010 Russian heat wave (Figs. 1, S1), making it the second most important driver of extreme temperature trends alongside the thermodynamic component (Fig. 4, Table 3). In contrast, no historical trend is observed for the 1972 Scandinavian heat wave (Figs. 2, S2), where extreme temperature trends are primarily driven by the interaction component and secondarily by the thermodynamic term (Fig. 5, Table 4). Once again, except for MPI-ESM1-2-LR, most models underestimate the observed analogue trends by exhibiting near-zero or negative ensemble-mean values, and only partially reproduce the partition of extreme temperature trends observed during the historical period.

Unlike the 2003 French event, inter-model differences persist in future projections. While most models project positive trends for atmospheric analogues associated with the 2010 Russian and 1972 Scandinavian heat waves, the MPI-ESM1-2-LR model generally shows negative values. Despite these differences, all models agree on an increase in extreme temperature occurrences associated with these analogues. For most models, this increase will be driven by all components, with the interaction term being the primary contributor, followed by the thermodynamic and dynamic terms. In contrast, the MPI-ESM1-2-LR model attributes the increase solely to the thermodynamic component. Finally, similar to the 2003 French event, trend partition analysis indicates that the thermodynamic (dynamic) term will become less (more) relevant compared to the past for both the events, while the role of the interaction term will be more and less important for the 2010 Russian and 1972 Scandinavian events, respectively.

Within the trend partition analysis, we further show that the large interaction term simulated for all three events in the projection period will be mainly driven by co-evolving long-term trends in the thermodynamic and dynamic components (Fig. 7, Table 6, Figs. S13–S14, Tables S1–S2). In contrast, its contribution most directly related to thermodynamic–dynamic covariability will be comparatively smaller, and does not show a robust relationship with land–atmosphere coupling as assessed here (Fig. 8), partly in contrast to suggestions in previous studies (e.g., Rogers et al. 2022). This prevents to draw definitive conclusions on the role of land–atmosphere coupling in driving changes in extreme temperature occurrences and, consistent with the concerns raised by Sui et al. (2020), calls for caution when providing physical interpretation to the interaction term.

In conclusion, the present study shows that the summer extreme temperature occurrences associated with specific atmospheric circulations increased during the historical period, and are projected to rise at an accelerated rate in the future. However, the drivers of these trends vary across Europe and over time. Indeed, the thermodynamic and dynamic changes were the primary drivers for historical trends associated with the 2010 Russian and 2003 French heat waves, consistent with an increase in their atmospheric analogue frequency. In contrast, the historical trends associated with the 1972 Scandinavian heat wave were mainly driven by thermodynamic and interaction terms, with no significant changes in its analogue frequency. In this context, models have been shown to underestimate atmospheric changes during the historical period, improperly capturing the drivers of historical extreme temperature trends. Looking ahead, models generally project further increases in extreme temperature occurrences associated with these analogues, with the projected trends primarily driven by the interaction term, which mainly reflects the strong co-evolving trends in the thermodynamic and dynamic components. However, these findings should be interpreted with caution due to inter-model differences and internal climate variability that reduce the reliability of future projections, particularly for extreme temperature occurrences in eastern and northern Europe. Conversely, future trends in extreme temperature occurrences in western and central Europe are associated with much lower uncertainty, as models consistently project similar results.

Future research should prioritize identifying the sources of model underestimation of historical atmospheric changes as in observational datasets. Additionally, efforts should aim to deepen the understanding of land–atmosphere coupling processes, which may vary across Europe and be not limited to soil moisture-related feedbacks. Addressing these issues is particularly crucial given the projected future increase in extreme temperature occurrences, where atmospheric dynamics and land–atmosphere coupling may play a more significant role compared to the past.

Supplementary Information The online version contains supplementary material available at https://doi.org/10.1007/s00382-026-08171-7.

Acknowledgements LFP, SP, PR, EB and SDS were supported by Horizon Europe Project "SoluTion foR mItiGatinG climate-induced hEalth thReats"–TRIGGER (CUP J33C22002420005).

Funding Open access funding provided by Alma Mater Studiorum - Università di Bologna within the CRUI-CARE Agreement.

Data availability ERA5 reanalysis data are available on Copernicus Climate Data Store (CDS), here: https://cds.climate.copernicus.eu/#!/search?text=ERA5. Data from the three CMIP5 models in Table 1 are available on the MMLE Archive (MMLEA) of the National Center for Atmospheric Research (NCAR), here: https://rda.ucar.edu/datasets/d651014/. Data from the three CMIP6 models in Table 1 are available on various nodes of the Earth System Grid Federation (ESGF), such as https://aims2.llnl.gov/. The daily NAO index is provided by the National Oceanic and Atmospheric Administration, here: https://ftp.cpc.ncep.noaa.gov/cwlinks/norm.daily.nao.index.b500101.current.ascii.

Declarations

Conflicts of interest The authors declare that they have no relevant financial or non-financial interests to disclose.

References

Barnes EA (2013) Revisiting the evidence linking Arctic amplification to extreme weather in midlatitudes. Geophys Res Lett 40(17):4734–4739

Barnes EA, Dunn-Sigouin E, Masato G, Woollings T (2014) Exploring recent trends in Northern Hemisphere blocking. Geophys Res Lett 41(2):638–644

Barriopedro D, Fischer EM, Luterbacher J, Trigo RM, García-Herrera R (2011) The hot summer of 2010: redrawing the temperature record map of Europe. Science 332(6026):220–224

Beverley JD, Woolnough SJ, Baker LH, Johnson SJ, Weisheimer A, O'Reilly CH (2021) Dynamical mechanisms linking Indian monsoon precipitation and the circumglobal teleconnection. Clim Dyn 57(9):2615–2636

Black E, Blackburn M, Harrison G, Hoskins B, Methven J (2004) Factors contributing to the summer 2003 European heatwave. Weather 59(8):217–223

Cai F, Liu C, Gerten D, Yang S, Zhang T, Li K, Kurths J (2024) Sketching the spatial disparities in heatwave trends by changing atmospheric teleconnections in the Northern Hemisphere. Nat Commun 15(1):8012

Cassano JJ, Uotila P, Lynch AH, Cassano EN (2007) Predicted changes in synoptic forcing of net precipitation in large Arctic river basins during the 21st century. J Geophys Res Biogeosciences 112 (G4)

Cassou C, Terray L, Phillips AS (2005) Tropical Atlantic influence on European heat waves. J Clim 18(15):2805–2811

Coumou D, Di Capua G, Vavrus S, Wang L, Wang S (2018) The influence of Arctic amplification on mid-latitude summer circulation. Nat Commun 9(1):2959

Davini P, D'Andrea F (2020) From CMIP3 to CMIP6: Northern Hemisphere atmospheric blocking simulation in present and future climate. J Clim 33(23):10021–10038

Delhaye S, Fichefet T, Massonnet F, Docquier D, Msadek R, Chripko S, Roberts C, Keeley S, Senan R (2021) Summertime changes in climate extremes over the peripheral Arctic regions after a sudden sea ice retreat. Weather Clim Dyn Discuss 2021:1–30

Deser C, Lehner F, Rodgers KB, Ault T, Delworth TL, DiNezio PN, Fiore A, Frankignoul C, Fyfe JC, Horton DE et al (2020) Insights from Earth system model initial-condition large ensembles and future prospects. Nat Clim Chang 10(4):277–286

Domeisen DIV, Eltahir EAB, Fischer EM, Knutti R, Perkins-Kirkpatrick SE, Schär C, Seneviratne SI, Weisheimer A, Wernli H (2023) Prediction and projection of heatwaves. Nat Rev Earth Environ 4(1):36–50

Donat MG, Pitman AJ, Seneviratne SI (2017) Regional warming of hot extremes accelerated by surface energy fluxes. Geophys Res Lett 44(13):7011–7019

Drijfhout S, Van Oldenborgh GJ, Cimatoribus A (2012) Is a decline of AMOC causing the warming hole above the North Atlantic in observed and modeled warming patterns? J Clim 25(24):8373–8379

Duchez A, Frajka-Williams E, Josey SA, Evans DG, Grist JP, Marsh R, McCarthy GD, Sinha B, Berry DI, Hirschi JJM (2016) Drivers of exceptionally cold North Atlantic Ocean temperatures and their link to the 2015 European heat wave. Environ Res Lett 11(7):074004.

Ebi KL, Capon A, Berry P, Broderick C, de Dear R, Havenith G, Honda Y, Kovats RS, Ma W, Malik A et al (2021) Hot weather and heat extremes: health risks. Lancet 398(10301):698–708.

Ehsan MA, Nicolì D, Kucharski F, Almazroui M, Tippett MK, Bellucci A, Ruggieri P, Kang I-S (2020) Atlantic ocean influence on middle East summer surface air temperature. NPJ Clim Atmos Sci 3(1):5

Famooss Paolini L, Athanasiadis PJ, Ruggieri P, Bellucci A (2022) The atmospheric response to meridional shifts of the Gulf Stream SST front and its dependence on model resolution. J Clim 35(18):6007–6030

Famooss Paolini L, Ruggieri P, Pascale S, Brattich E, Di Sabatino S (2024) Hybrid statistical–dynamical seasonal prediction of summer extreme temperatures in Europe. Q J R Meteorol Soc 151(766):e4900

Fischer EM, Seneviratne SI, Lüthi D, Schär C (2007) Contribution of land-atmosphere coupling to recent European summer heat waves. Geophysical Research Letters, 34(6)

Fragkoulidis G, Wirth V, Bossmann P, Fink A (2018) Linking Northern Hemisphere temperature extremes to Rossby wave packets. Q J R Meteorol Soc 144(711):553–566

Francis JA, Vavrus SJ (2012) Evidence linking Arctic amplification to extreme weather in mid-latitudes. Geophys Res Lett 39(6)

García-Herrera R, Díaz J, Trigo RM, Luterbacher J, Fischer EM (2010) A review of the European summer heat wave of 2003. Crit Rev Environ Sci Technol 40(4):267–306

Hamed KH, Rao AR (1998) A modified Mann-Kendall trend test for autocorrelated data. J Hydrol 204(1–4):182–196

Hegerl GC, Ballinger AP, Booth BBB, Borchert LF, Brunner L, Donat MG, Doblas-Reyes FJ, Harris GR, Lowe J, Mahmood R et al (2021) Toward consistent observational constraints in climate predictions and projections. Front Climat 3(678):109

Hersbach H, Bell B, Berrisford P, Hirahara S, Horányi A, Muñoz-Sabater J, Nicolas J, Peubey C, Radu R, Schepers D et al (2020) The ERA5 global reanalysis. Q J R Meteorol Soc 146(730):1999–2049.

Holmes CR, Woollings T, Hawkins E, De Vries H (2016) Robust future changes in temperature variability under greenhouse gas forcing and the relationship with thermal advection. J Clim 29(6):2221–2236

Horton DE, Johnson NC, Singh D, Swain DL, Rajaratnam B, Diffenbaugh NS (2015) Contribution of changes in atmospheric circulation patterns to extreme temperature trends. Nature 522(7557):465–469

Horton RM, Mankin JS, Lesk C, Coffel E, Raymond C (2016) A review of recent advances in research on extreme heat events. Current Climate Change Reports 2:242–259

Hussain M, Mahmud I (2019) pymannkendall: a python package for non parametric Mann Kendall family of trend tests. J Open Source Softw 4(39):1556

Jézéquel A, Cattiaux J, Naveau P, Radanovics S, Ribes A, Vautard R, Vrac M, Yiou P (2018) Trends of atmospheric circulation during singular hot days in Europe. Environ Res Lett 13(5):054007

Jézéquel A, Yiou P, Radanovics S (2018) Role of circulation in European heatwaves using flow analogues. Clim Dyn 50(3):1145–1159

Katzenberger A, Schewe J, Pongratz J, Levermann A (2020) Robust increase of Indian monsoon rainfall and its variability under future warming in CMIP-6 models. Earth Syst Dyn Discuss 2020:1–30

Kay JE, Deser C, Phillips A, Mai A, Hannay C, Strand G, Arblaster JM, Bates SC, Danabasoglu G, Edwards J et al (2015) The community earth system model (CESM) large ensemble project: a community resource for studying climate change in the presence of internal climate variability. Bull Am Meteor Soc 96(8):1333–1349

Kirchmeier-Young MC, Zwiers FW, Gillett NP (2017) Attribution of extreme events in Arctic sea ice extent. J Clim 30(2):553–571

Knutti R, Furrer R, Tebaldi C, Cermak J, Meehl GA (2010) Challenges in combining projections from multiple climate models. J Clim 23(10):2739–2758

Kornhuber K, Petoukhov V, Petri S, Rahmstorf S, Coumou D (2017) Evidence for wave resonance as a key mechanism for generating high-amplitude quasi-stationary waves in boreal summer. Clim Dyn 49:1961–1979

Kornhuber K, Osprey S, Coumou D, Petri S, Petoukhov V, Rahmstorf S, Gray L (2019) Extreme weather events in early summer 2018 connected by a recurrent hemispheric wave-7 pattern. Environ Res Lett 14(5):054002

Koster RD, Chang Y, Wang H, Schubert SD (2016) Impacts of local soil moisture anomalies on the atmospheric circulation and on remote surface meteorological fields during boreal summer: a comprehensive analysis over North America. J Clim 29(20):7345–7364

Lee J-Y, Marotzke J, Bala G, Cao L, Corti S, Dunne JP, Engelbrecht F, Fischer E, Fyfe JC, Jones C, others (2021) Future global climate: scenario-based projections and near-term information. Climate change 2021: The physical science basis. Contribution of working group I to the sixth assessment report of the intergovernmental panel on climate change, Cambridge University Press, pp. 553–672

Lee H, Calvin K, Dasgupta D, Krinner G, Mukherji A, Thorne P, Trisos C, Romero J, Aldunce P, Barrett K, others (2023) Climate change 2023 synthesis report. Contribution of working groups I, II and III to the sixth assessment report of the intergovernmental panel on climate change. The Australian National University

Li J, Tam C-Y, Tai AP, Lau N-C (2021) Vegetation-heatwave correlations and contrasting energy exchange responses of different vegetation types to summer heatwaves in the Northern Hemisphere during the 1982–2011 period. Agric For Meteorol 296(108):208

Maher N, Milinski S, Ludwig R (2021) Large ensemble climate model simulations: introduction, overview, and future prospects for utilising multiple types of large ensemble. Earth Syst Dyn 12(2):401–418

Mamalakis A, Randerson JT, Yu J-Y, Pritchard MS, Magnusdottir G, Smyth P, Levine PA, Yu S, Foufoula-Georgiou E (2021) Zonally contrasting shifts of the tropical rain belt in response to climate change. Nat Clim Chang 11(2):143–151

Mann ME, Rahmstorf S, Kornhuber K, Steinman BA, Miller SK, Coumou D (2017) Influence of anthropogenic climate change on planetary wave resonance and extreme weather events. Sci Rep 7(1):1–12

Masselot P, Mistry MN, Rao S, Huber V, Monteiro A, Samoli E, Stafoggia M, de'Donato F, Garcia-Leon D, Ciscar J-C, others (2025) Estimating future heat-related and cold-related mortality under climate change, demographic and adaptation scenarios in 854 European cities. Nature Medicine, 1–9

Nabat P, Somot S, Mallet M, Sanchez-Lorenzo A, Wild M (2014) Contribution of anthropogenic sulfate aerosols to the changing Euro-Mediterranean climate since 1980. Geophys Res Lett 41(15):5605–5611

Nicolì D, Bellucci A, Iovino D, Ruggieri P, Gualdi S (2020) The impact of the AMV on Eurasian summer hydrological cycle. Sci Rep 10(1):14444

Olonscheck D, Suarez-Gutierrez L, Milinski S, Beobide-Arsuaga G, Baehr J, Fröb F, Ilyina T, Kadow C, Krieger D, Li H, others (2023) The new max planck institute grand ensemble with CMIP6 forcing and high-frequency model output. J Adv Model Earth Syst. 15(10):e2023MS003790

Overpeck JT, Udall B (2020) Climate change and the aridification of North America. Proc Natl Acad Sci 117(22):11856–11858

Peings Y, Cattiaux J, Vavrus S, Magnusdottir G (2017) Late twenty-first-century changes in the midlatitude atmospheric circulation in the CESM large ensemble. J Clim 30(15):5943–5960

Petoukhov V, Rahmstorf S, Petri S, Schellnhuber HJ (2013) Quasiresonant amplification of planetary waves and recent Northern Hemisphere weather extremes. Proc Natl Acad Sci 110(14):5336–5341

Riboldi J, Lott F, d'Andrea F, Rivière G (2020) On the linkage between Rossby wave phase speed, atmospheric blocking, and Arctic amplification. Geophys Res Lett 47(19):e2020GL087796

Rogers CD, Kornhuber K, Perkins-Kirkpatrick SE, Loikith PC, Singh D (2022) Sixfold increase in historical Northern Hemisphere concurrent large heatwaves driven by warming and changing atmospheric circulations. J Clim 35(3):1063–1078

Röthlisberger M, Papritz L (2023) Quantifying the physical processes leading to atmospheric hot extremes at a global scale. Nat Geosci 16(3):210–216

Rousi E, Kornhuber K, Beobide-Arsuaga G, Luo F, Coumou D (2022) Accelerated western European heatwave trends linked to more-persistent double jets over Eurasia. Nat Commun 13(1):3851

Rousi E, Fink AH, Andersen LS, Becker FN, Beobide-Arsuaga G, Breil M, Cozzi G, Heinke J, Jach L, Niermann D et al (2023) The extremely hot and dry 2018 summer in central and northern Europe from a multi-faceted weather and climate perspective. Nat Hazard 23(5):1699–1718

Ruckstuhl C, Philipona R, Behrens K, Collaud Coen M, Dürr B, Heimo A, Mätzler C, Nyeki S, Ohmura A, Vuilleumier L, others (2008) Aerosol and cloud effects on solar brightening and the recent rapid warming. Geophys Res Lett 35(12)

Ruggieri P, Kucharski F, Buizza R, Ambaum M (2017) The transient atmospheric response to a reduction of sea-ice cover in the Barents and Kara Seas. Q J R Meteorol Soc 143(704):1632–1640

Russo S, Sillmann J, Fischer EM (2015) Top ten European heatwaves since 1950 and their occurrence in the coming decades. Environ Res Lett 10(12):124003

Ruti PM, Dell'Aquila A, Giorgi F (2014) Understanding and attributing the Euro-Russian summer blocking signatures. Atmos Sci Lett 15(3):204–210

Seneviratne SI, Lüthi D, Litschi M, Schär C (2006) Land-atmosphere coupling and climate change in Europe. Nature 443(7108):205–209

Seneviratne SI, Corti T, Davin EL, Hirschi M, Jaeger EB, Lehner I, Orlowsky B, Teuling AJ (2010) Investigating soil moisture-climate interactions in a changing climate: a review. Earth Sci Rev 99(3–4):125–161

Serreze MC, Barry RG (2011) Processes and impacts of Arctic amplification: a research synthesis. Global Planet Change 77(1–2):85–96

Shepherd TG (2014) Atmospheric circulation as a source of uncertainty in climate change projections. Nat Geosci 7(10):703–708

Sinclair VA, Mikkola JW, Rantanen M, Raisanen J (2019) The summer 2018 heatwave in Finland. Weather 74(11):403–409

Suarez-Gutierrez L, Müller WA, Li C, Marotzke J (2020) Dynamical and thermodynamical drivers of variability in European summer heat extremes. Clim Dyn 54:4351–4366

Sui C, Yu L, Vihma T (2020) Occurrence and drivers of wintertime temperature extremes in Northern Europe during 1979–2016. Tellus A Dyn Meteorol Oceanogr 72(1):1–19

Sun C, Li J, Zhao S (2015) Remote influence of Atlantic multidecadal variability on Siberian warm season precipitation. Sci Rep 5(1):16853

Sun L, Alexander M, Deser C (2018) Evolution of the global coupled climate response to Arctic sea ice loss during 1990–2090 and its contribution to climate change. J Clim 31(19):7823–7843

Swart NC, Cole JNS, Kharin VV, Lazare M, Scinocca JF, Gillett NP, Anstey J, Arora V, Christian JR, Hanna S, others (2019) The Canadian earth system model version 5 (CanESM5. 0.3). Geosci Model Dev 12(11):4823–4873

Teng H, Branstator G, Tawfik AB, Callaghan P (2019) Circumglobal response to prescribed soil moisture over North America. J Clim 32(14):4525–4545

Teuling AJ, Seneviratne SI, Stöckli R, Reichstein M, Moors E, Ciais P, Luyssaert S, Van Den Hurk B, Ammann C, Bernhofer C et al (2010) Contrasting response of European forest and grassland energy exchange to heatwaves. Nat Geosci 3(10):722–727

Trenberth KE, Fasullo JT (2012) Climate extremes and climate change: The Russian heat wave and other climate extremes of 2010. J Geophys Res Atmos 117(D17)

Vautard R, Cattiaux J, Happé T, Singh J, Bonnet R, Cassou C, Coumou D, D'andrea F, Faranda D, Fischer E et al (2023) Heat extremes in Western Europe increasing faster than simulated due to atmospheric circulation trends. Nat Commun 14(1):6803

Vogel MM, Orth R, Cheruy F, Hagemann S, Lorenz R, van den Hurk BJ, Seneviratne SI (2017) Regional amplification of projected changes in extreme temperatures strongly controlled by soil moisture-temperature feedbacks. Geophys Res Lett 44(3):1511–1519

Vogel MM, Zscheischler J, Seneviratne SI (2018) Varying soil moisture-atmosphere feedbacks explain divergent temperature extremes and precipitation projections in central Europe. Earth Syst Dyn 9(3):1107–1125

Wang H, Schubert SD, Koster RD, Chang Y (2019) Phase locking of the boreal summer atmospheric response to dry land surface anomalies in the Northern Hemisphere. J Clim 32(4):1081–1099

Weller E, Cai W, Min S-K, Wu L, Ashok K, Yamagata T (2014) More-frequent extreme northward shifts of eastern Indian Ocean tropical convergence under greenhouse warming. Sci Rep 4(1):6087

Wolf G, Brayshaw DJ, Klingaman NP, Czaja A (2018) Quasi-stationary waves and their impact on European weather and extreme events. Q J R Meteorol Soc 144(717):2431–2448

Woollings T, Barriopedro D, Methven J, Son S-W, Martius O, Harvey B, Sillmann J, Lupo AR, Seneviratne S (2018) Blocking and its response to climate change. Curr Clim Change Rep 4:287–300

Wyser K, Koenigk T, Fladrich U, Fuentes-Franco R, Karami MP, Kruschke T (2021) The SMHI large ensemble (SMHI-LENS) with EC-earth3. 3.1. Geosci Model Dev 14(7):4781–4796

Xu P, Wang L, Vallis GK, Geen R, Screen JA, Wu P, Ding S, Huang P, Chen W (2021) Amplified waveguide teleconnections along the polar front jet favor summer temperature extremes over northern Eurasia. Geophys Res Lett 48(13):e2021GL093735

Yiou P, Cattiaux J, Faranda D, Kadygrov N, Jézéquel A, Naveau P, Ribes A, Robin Y, Thao S, van Oldenborgh GJ et al (2020) Analyses of the Northern European summer heatwave of 2018. Bull Am Meteor Soc 101(1):S35–S40

Yoon D, Chen J-H, Hsu H, Findell KL (2026) Variations in land-atmosphere coupling during drought-heatwave events. Commun Earth Environ 7(1):1